REMOTE SENSING WITH AIRBORNE INFRARED THERMOGRAPHY FOR ASSESSMENT OF LANDSCAPE SCALE WILDFIRE SPREAD AND INTENSITY

A Thesis

Presented To

The Faculty of the Department of Meteorology and Climate Science

San José State University

In Partial Fulfillment

of the Requirement of the Degree

Master of Science

by

Christopher Charles Giesige

May 2024

The Designated Thesis Committee Approves the Thesis Titled

REMOTE SENSING WITH AIRBORNE INFRARED THERMOGRAPHY FOR ASSESSMENT OF LANDSCAPE SCALE WILDFIRE SPREAD AND INTENSITY

by

Christopher Charles Giesige

APPROVED FOR THE DEPARTMENT OF METEOROLOGY AND CLIMATE SCIENCE

SAN JOSÉ STATE UNIVERSITY

May 2024

Craig Clements, Ph.D.	Department of Meteorology and Climate Science
Adam Kochanski, Ph.D.	Department of Meteorology and Climate Science
Miguel Valero, Ph.D.	Department of Fluid Mechanics, Universitat Politècnica de Catalunya, Barcelona, Spain

ABSTRACT

REMOTE SENSING WITH AIRBORNE INFRARED THERMOGRAPHY FOR ASSESSMENT OF LANDSCAPE SCALE WILDFIRE SPREAD AND INTENSITY

by Christopher Charles Giesige

Wildland fire is one of the most complex environmental physical processes to quantify. The way in which we observe and measure wildland fire is critical in understanding how these processes drive fire dynamics. Fire behavior can be observed in several ways including the use of ground sensors and remote sensing packages aboard aircraft and satellites. Airborne sensors provide high spatial resolution and can provide high temporal resolution. Infrared thermography takes advantage of radiant heat transfer allowing for the study of fire characteristics such as fire spread and intensity. Aircraft observations utilizing infrared cameras have been a well-established method of fire observation, yet there is still a significant lack of comprehensive data available. Presented in this research are several advances in the use of infrared remote sensing techniques to evaluate fire behavior. First, a synthesis of knowledge and methods regarding the use of infrared camera systems to measure fire behavior is discussed and analyzed. Second, is the use of airborne infrared data collected during tactical firefighting operations to develop an automated method of extracting active fire edges for fire spread analysis. Third, is an analysis of high-resolution fire behavior data collected during several wildfires in the 2022 fire season and the new methods used to process the images, calculate fire radiative power, and evaluate fire spread. These methods are a contribution to the advancement of being able to use operational firefighting data for research applications, furthering automated methods of processing large data quantities to evaluate fire spread, and evaluating high-resolution landscape scale wildfire behavior.

ACKNOWLEDGMENTS

First, I would like to thank my advisor Dr. Valero for his mentoring and patience throughout the program especially while I was learning this new set of skills in data analysis. I greatly appreciate the opportunity I have had to work with state-of-the-art fire behavior equipment and first-ever datasets. Along with Dr. Valero, I would also like to thank Dr. Clements for bringing me into the program, providing me with the opportunity to participate in the great field research opportunities that we had, and guidance throughout the graduate program. I would like to thank Dr. Kochanski for his help and guidance in understanding data analysis methods and research applications.

Furthermore, I would like to thank team members Andrew Klofas and Eric Goldbeck-Dimon for all of their efforts and help. Our airborne camera system would not have been as sophisticated as it was without Andrew's amazing skill in engineering and programming, and my analysis of active fire perimeters would not have been as extensive without Eric's great ability to work with GIS.

I would also like to thank Cal Fire for sharing their operational dataset to be used in research as it has a lot of potential to be used for future groundbreaking analysis of fire behavior, and the National Oceanic and Atmospheric Administration (NOAA) who allowed us to join their field campaign and fly our camera system aboard their aircraft.

Lastly, I would like to thank the Naval Research Laboratory (NRL), Dr. David Peterson, and Dr. Theodore McHardy for providing me the opportunity to intern at NRL, work with Dr. Pederson and Dr. McHardy on their groundbreaking research into fire behavior, and gain a few new skillsets in fire research.

TABLE OF CONTENTS

List of Tables………………………………………………………………………. viii

List of Figures……………………………………………………………………... ix

List of Acronyms…………………………………………………………………... xii

1 Synthesis of Knowledge and Methods Regarding the Use of Infrared Camera Systems to Measure Fire Radiative Properties and Rate of Spread……………… 1
  1.1 Introduction……………………………………………………………... 1
  1.2 Physics of remote sensing………………………………………………. 3
  1.3 Sensors and methods used in measuring fire radiative characteristics…….. 5
  1.4 Conclusion………………………………………………………………. 11

2 Automated Extraction of Active Fire Edges from Tactical Infrared Observations of Wildfire………………………………………………………………… 13
  2.1 Abstract……………………………………………………………..... 13
  2.2 Introduction……………………………………………………………… 14
  2.3 Background……………………………………………………………… 18
    2.3.1 Thresholding and edge detection…………………………………….. 18
    2.3.2 Morphological functions…………………………………………….... 19
    2.3.3 Structure analysis…………………………………………………….. 19
  2.4 Methods………………………………………………………………….. 20
    2.4.1 Remote sensing data………………………………………………….. 20
    2.4.2 Thresholding and edge detection processing…………………………. 21
      2.4.2.1 Canny edge detector……………………………………………. 23
      2.4.2.2 OTSU’s binarization followed by Canny edge detector……….. 24
      2.4.2.3 Multi-thresholding followed by Canny edge detector………… 24
      2.4.2.4 Alternate intensity thresholding……………………………….... 25
    2.4.3 Polygon functions…………………………………………………….. 27
  2.5 Results……………………………………………………………………. 28
    2.5.1 Automated methods comparison……………………………………… 28
    2.5.2 Application of automated method…………………………………….. 32
    2.5.3 Performance metrics………………………………………………….... 36
  2.6 Discussion and conclusion……………………………………………….. 42

3 Analysis of High-Resolution Airborne Thermal Infrared Fire Behavior Data Collected During the California Fire Dynamics Experiment (CALFIDE)………… 46
  3.1 Abstract………………………………………………………………….. 46
  3.2 Introduction……….……………………………………………………… 46
  3.3 Methods………………………………………………………………….. 49
    3.3.1 Fire observations..……………………………………………………... 49
    3.3.2 Data processing………………………………………………………… 50

3.3.2.1 Mountain fire - sensor integration, georeferencing, and FRP…… 50
3.3.2.2 Mosquito fire – automated edge detection……………………… 54
3.4 Results……………………………………………………………….. 56
3.4.1 Mountain fire, georeferencing and FRP………………………………. 56
3.4.2 Mosquito fire, delineating active fire edges…………………………… 61
3.5 Conclusion and discussion…………………………………………... 64
3.6 Future work………………………………………………………….. 65

4 Conclusion……………………………………………………………………. 67

References………………………………………………………………………… 69

LIST OF TABLES

Table 1 Five evaluation metrics used to assess the performance of the automated method. Baddeley distance, FOM, Inner/Outer difference, Jaccard index, and Area…………………………………………….......................... 40

Table 2 Calculated maximum FRP values for each pass over the Mountain fire………………………………………………………………………… 60

LIST OF FIGURES

Figure 1 Four LWIR images captured during the 2020 Oak (a, b, c) and Glass (d) fires in California, USA. Pixels that are darker are lower in intensity representative of background values and lower intensity fire, whereas pixels that are white are of higher intensity representative of more intense areas of the fire. These images provide a good representation of how the fire geometries and fire area intensities can vary by image……………………… 22

Figure 2 Progression of the processes involved in contouring active fire edges. a) is the original LWIR image, b) is the output of applying the threshold mask utilizing equation (8), c) is an output of the threshold mask after applying morphological operations, and d) displays the final output when applying the canny edge detector and removing unwanted edges. b) provides a good example of why morphological operations are necessary after applying a threshold mask given the gaps along the edge of the fire area. Looking at c), gaps in the active fire edge and area have diminished leaving a more continuous edge to be contoured..………………………………………….. 27

Figure 3 Block diagram of the image processing methods and techniques showing the order of operations. Black boxes are the input and output, purple boxes represent the initial step for each method, blue ovals are the main thresholding or edge detection algorithm used, green soft rectangles are secondary analysis tools such as morphological operators, and the orange hectogon signifies the final step of detecting the active fire edge…………... 27

Figure 4 Four methods of extracting active fire edges are compared against each other and to the original LWIR image. There is a clear distinction between the performance of the fourth method compared to the other three. Mean threshold plus canny edge detection is able to capture active fire edges throughout the diverse fire intensities and geometries……………………… 31

Figure 5 The original image (left) captures a distinct active fire edge extending from the top of the frame to the bottom of the frame, with a few spotting fire pixels along the right border. After the mean threshold with canny edge detection is applied (right), the method does not delineate the continuous active fire edge that can be picked out in the original image (left). Rather it follows gaps in the higher-intensity regions, not accounting for edges mixed with lower-intensity areas..………………………………………………. 32

Figure 6 A mosaic of the automated method applied to binary individual georeferenced single flight images during the Oak fire. When applied to individual images the algorithm characterizes more detail in the shape of the active fire edge, but segments the main fire area into multiple fire areas………………………………………………………………………… 33

Figure 7 a) Mosaic of a single flight taken during the Oak fire (flight 0533), b) when the automated algorithm is applied to a single flight mosaic, and c) mosaic manually annotated active fire edge. When applied to the mosaic (b) a single continuous polygon is created in the main fire area and the double edging is diminished…………………………………………………….. 35

Figure 8 Area differencing between the automated edged delineation and manual annotation delineation of the active fire edge. Areas shaded in pink are the outer difference between the automated and manual methods, and purple is the inner difference……………………………………………………… 41

Figure 9 The four flights used in evaluation metrics: a) the Oak fire flight 0533, b) Oak fire flight 0535, c) Oak fire flight 0537, and d) Slater fire flight 0553. Each image provides a visualization of the automated method applications. The blue dotted line represents the results of applying the automated method directly, the yellow line is after applying the concave hull, and the brown line is the hand-drawn annotation………………………………… 42

Figure 10 The NOAA Twin Otter (left), and a display of the SWIS instrument aboard the Twin Otter (right). The instrument points out the bottom of the aircraft providing a nadir view of the fire……………………………………….... 49

Figure 11 Example of LWIR images (a,b) captured from the Workswell camera and a MWIR image (c) captured from the Telops camera taken during the Mountain fire…………………………………………………………….. 51

Figure 12 Shows the flight paths (green) taken during the analysis period over the fire perimeters of the Mountain fire (left) and Mosquito fire (right). The darker red perimeters are the fire perimeters on the day of observation and the brighter red perimeters indicate the growth of the fires into the following day……………………………... 52

Figure 13 Frames from a single pass over the active fire edge are aligned with tie points (white, gray, and black dots) projected onto a basemap in the Metashape software…………………………………………………... 53

Figure 14 Block diagram of the automated method developed for the high-resolution LWIR image mosaics during the Mosquito fire. The input image is a long-wave thermal orthomosaic where a Gaussian filter was first applied, followed by the canny edge detector to detect the active fire edges, and then connecting the edge contours……….. 56

Figure 15 Orthomosaic of MWIR images captured during the Mountain fire. A mosaic raster is produced distorting the fire pixels in the image giving the active fire edge and area a smeared appearance. ……….. 57

Figure 16 LWIR orthomosaics of four passes over the fire: a) pass 1, b) pass 2, c) pass 4, and d) pass 7. Images are properly aligned without distortion to the shape or size of the fire……………………………………………………….. 58

Figure 17 Orthomosaics of the ten passes over the fire show the evolution of the fire spread on 09-03-2022 from 22:59:23 – 23:54:34UTC (1559 to 1654 local time). Darker colors indicate lower pixel intensities and brighter white pixels indicate higher pixel intensities. The middle and bottom regions of the fire expanded west/southwestward exhibiting significant fire growth during the 55 minutes of observation……………………………………… 59

Figure 18 Example LWIR FRP values plotted during pass 1, pass 8, and pass 10 over the Mountain fire 09-03-2022. Higher FRP corresponds to higher intensity areas of the fire along the active fire edge. The FRP value ranges were plotted for visual representation so higher intensity aspects of the fire are clearly displayed..………………………………………………………. 61

Figure 19 The automated active fire edge method applied to georeferenced flight mosaics. Each mosaic represents one pass over the same fire edge. The algorithm successfully delineated the active fire edge in the eight passes………………………………………………………………… 63

LIST OF ACRONYMS

AMS	Autonomous Modular Sensor
BIRD	Bi-Spectral Infrared Detection
BT	Brightness Temperature
CALFIDE	California Fire Dynamics Experiment
CSL	Chemical Sciences Laboratory
DEM	Digital Elevation Model
FIREX-AQ	Fire Influence on Regional to Global Environment on Air Quality
FOM	Figure of Merrit
FRE	Fire Radiative Energy
FRED	Fire Radiative Energy Density
FRP	Fire Radiative Power
FRPD	Fire Radiative Power Density
GIS	Geographic Information Systems
GOES	Geostationary Operational Environment Satellite
INS	Inertial Navigation System
IR	Infrared
LTM	Landsat Thematic Mapper
LWIR	Long Wave Infrared
MASTER	MODIS/ASTER Airborne Simulator
MIR	Mid-Infrared

MODIS	Moderate Resolution Infrared Sensor
MWIR	Mid Wave Infrared
NASA	National Aeronautics and Space Administration
NDBR	Normalized Difference Burn Ratio
NDVI	Normalized Difference Vegetation Index
NIFC	National Interagency Fire Center
NIR	Near Infrared
NOAA	National Oceanic and Atmospheric Administration
ROS	Rate of Spread
RPAS	Remotely Piloted Aircraft System
RxCADRE	Prescribed Fire Combustion and Atmospheric Dynamics Research Experiment
SJSU	San Jose State University
SWIR	Short Wave Infrared
SWIS	San Jose State Wildfire Infrared System
TIROS-N	Televisons and Infra-Red Obsertation Satellite -N
USGS	United States Geological Survey
VIIRS	Visible Infrared Imaging Radiometer Suite
VHRR	Very High Resolution Radiometer
WASP	Wildfire Airborne Sensor Program

Chapter 1

Synthesis of Knowledge and Methods Regarding the Use of Infrared Camera Systems to Measure Fire Radiative Properties and Rate of Spread

1.1 Introduction

Wildland or vegetation fires are non-structure fires that burn in natural fuels and can be distinguished into two types: prescribed fire used for ecosystem management and field experiments, and wildfires which are unplanned fires with ignitions from human or lightning causes. Fire research during both prescribed fires and wildfires have been used to model the benefits and effects fires have in an ecosystem, how they interact with surrounding environments and atmospheres, and how they impact our society. During the past several decades advances in our knowledge of wildland fires have administered improved fire behavior modeling efforts utilizing fire's heat transfer mechanisms as a major component.

Remote sensing has become an established and increasingly popular method to study wildland fires by means of observing radiant energy (radiant heat) produced by the fire, where the radiative component can be effectively measured. The use of remote sensing to evaluate distinct active fire properties can fall into two main applications: detecting actively burning areas and estimating radiative energy from thermal imagery (Lentile et al. 2006). Current research uses infrared sensors tailored to the mid-wave and long-wave portion of the infrared spectrum (Wooster et al. 2013, O'Brien et al. 2016) as these wavelengths are most useful for active fire detection over a range of fire temperatures and intensities (low intensity/smoldering and high intensity), identifying fire fronts, estimating the amount of fuel combusted, and smoke emissions. Remote sensing methods, especially at higher resolution, can be used to measure different fire behavior characteristics such as rate of spread (ROS) and spotting, the amount of biomass consumed, and quantifying fireline intensity (Riggan and Tissel 2009).

Several methods have been developed that utilize remote sensing to calculate the radiant energy release by a fire defined as the fire radiative power (FRP) (Wooster et al. 2005). When integrating FRP with time, the derived relationship is fire radiative energy (FRE). There are several ways of measuring FRP: by use of ground radiometers with nadir-viewing or oblique viewing angles mounted on platforms several meters off the ground (O'Brien et al. 2016), airborne sensors mounted on remotely piloted aircraft systems (RPAS) (Dickinson et al. 2016), fixed-wing and rotary aircraft (Paugam et al. 2013) with a specified viewing angle and lens, and spaceborne sensors attached to satellites. Most research using the FRP method has focused on the use of spaceborne sensors, using airborne and ground sensors to help validate spaceborne measurements, and identify different methods and approaches to measure fire characteristics. However, there is a need for both the collection of more high-resolution data and the collection of more data from landscape scale wildfires, as most airborne infrared data has been collected during prescribed fire experiments.

The absence of readily available high-resolution comprehensive wildfire datasets, along with the limitations in advanced methods to process those datasets, has hindered the progress of being able to accurately forecast fire behavior. The subsequent analyses in this paper aim to enhance the development of processing methodologies adept at discerning fire behavior characteristics from fire radiative properties across diverse wildfire datasets. Successful refinement of these processing methods will lead to more accurate estimations of active fire edge progression at fine scales and have the potential to contribute to the validation of numerical fire models.

1.2 Physics of remote sensing

Fire is an uncontrolled chemical reaction that undergoes a sustainable combustion process evolving from the heat and oxidation of a fuel source. Fire itself releases heat, light, and reactant products. The role of heat transfer mechanisms involves both sustaining combustion and the fire's interaction with the environment. In wildland fires, convection and radiation are the two significant heat transfer processes responsible for fire propagation and consumption of fuel sources, mainly vegetation.

Appropriate wavelengths to measure fire's radiative properties can be distinguished by the relationship between radiation intensity, wavelength, and temperature. Planck's Law describes the radiance absorption and emittance of an object considered to be a blackbody – an object superlative in absorbing and emitting all of the radiant energy provided to it. Planck's Law was derived from the relationship between energy and frequency at a given wavelength for all wavelengths using Planck's constant, which can be written in terms of blackbody emissive power (Zhang et al. 2016):

$$B_{\lambda,T} = \frac{2\pi hc^2}{\lambda^5} \cdot \frac{1}{exp^{\frac{hc}{\lambda k_B T}} - 1} \qquad (1)$$

where λ is the wavelength, h is Planck's constant 6.626×10^{-34} (m^2 kg / s), c is the speed of light, k_B is the Boltzmann constant 1.3808×10^{-23} (m^2 kg / s^2 K), and T is the absolute temperature. The spectral radiance by a blackbody with temperature (T) is (Johnson 2017)

$$B(\lambda, T) = \frac{C_1 \lambda^{-5}}{\pi(e^{C_2/\lambda T} - 1)} \qquad (2)$$

where C_1 and C_2 are the Planck constants 3.741832x10^{-16} (W/m^2) and 1.438786x10^{-2} (m·K).

This relationship can be used to determine the thermal and background radiance to calculate a fire's fractional area and its temperature within a pixel. With L_λ as the radiance at wavelength λ, f_{fire} is the fire fractional area, $f_{background}$ is the background fractional area, B(λ,T) is the Plank function, and $T_{background}$ is the temperature of the background (Dennison et al. 2006), the radiance can be calculated as,

$$L_\lambda = f_{fire}B\left(\lambda, T_{fire}\right) + f_{background}B(\lambda, T_{background}) \qquad (3)$$

The intensity that is emitted from an object depends on the temperature and wavelength of the radiated energy. Wien's Displacement Law expresses that the higher the amount of radiant heat emitted by an object, the shorter the wavelength it emits at and is given by:

$$\lambda_{max} \cdot T = b \qquad (4)$$

where λ_{max} is the wavelength of the emission peak, T is the absolute temperature, and b is the constant 2897.8 (μm K). Integration of Plank's Law provides a relationship between temperature and radiation emitted by an object established as the Stefan-Boltzmann Law,

$$E = \sigma T^4 \qquad (5)$$

where E is the energy flux, σ is the Stefan-Boltzmann constant 5.67x10^{-8} (W/m^2·K^4), and T is the absolute temperature (Zhang et al. 2016). Equations 1-5 are used to determine which spectral band passes to use in measuring wildland fires based on their temperatures.

Typical temperatures for wildland fires will range between 1000-1500K (Dennison et al. 2006), but temperatures from fires can vary from 675K for smoldering with observations extending to 1600K in the flaming front (Riggan et al. 2004, Wooster et al. 2005). Given these values, fire emits radiant energy in the visible (400-700 nm), near-infrared (NIR) (0.75-

1.0 µm), short-wave infrared (SWIR) (1-2.5 µm), mid-wave infrared (MWIR) (3-5 µm), and long-wave infrared (LWIR) (8-14 µm) bands of the electromagnetic spectrum. Remote sensing utilizes this knowledge to make observations in both the visible and infrared regions. However, several conditions need to be considered: the reflectance wavelengths of the fire background including vegetation, soil, and water; reflectance of solar radiation during the day; reflectance and emittance of combustion products such as hot gasses, aerosols, and smoke; and atmospheric absorption. Because of the background temperature and wavelengths emitted by other objects in the visible, NIR, and SWIR (hot gasses and soot), it is better suited to measure wildland fires using the MWIR and LWIR bands; although there is a strong emittance by CO_2 at 4.3µm (Johnston et al. 2014). MWIR allows for capturing fire at higher temperatures and peak emittance, while LWIR allows for capturing fires at more ambient temperatures (Allison et al. 2016) to be used in comparison with the MWIR band.

Measurements of wildland fires using spaceborne and airborne sensors account for so-called “atmospheric windows”, which reside due to the differences in absorptivity of certain wavelengths by atmospheric molecules. These windows are ranges where the atmosphere has the highest transparency and certain portions of the electromagnetic spectrum can penetrate the atmospheric layer. Most notable atmospheric windows lie within the visible to SWIR (~0.4-2.5µm), MWIR (~3.0-5.0 µm), and LWIR (~8.0-14.0 µm) (Agueda et al. 2010). As described earlier, these windows correspond appropriately with wavelengths detectible during wildland fires.

1.3 Sensors and methods used in measuring fire radiative characteristics

Use of remote sensing infrared thermography (Allison et al. 2016, Johnson 2017, Hulley et al. 2019) and its utilization aboard aircraft to detect and measure wildland fire dates to the 1960s (Wilson et al. 1971) where it was found that airborne infrared thermography was a useful approach to active fire detection. However, their use as a proponent for data collection and fire retrieval has been limited by their ability to be readily available.

Ground sensors with nadir-viewing or oblique viewing angles are also used in prescribed burns denoted as “true” surface values because of their proximity to surface conditions. They are used in lab and field experiments where the cameras can be mounted on towers or lifts and placed in the burn area location before fire ignition (O’Brien et al. 2016), but their use is also limited in wildfires as their placement needs to be established beforehand.

In contrast, the use of spaceborne sensors aboard satellites such as the National Aeronautics and Space Administration’s (NASA) Terra and Aqua Moderate Resolution Imaging Spectroradiometer (MODIS), the National Oceanic and Atmospheric Administration’s (NOAA) Visible Infrared Imaging Radiometer Suite (VIIRS), and NOAA’s Geostationary Operational Environmental Satellite (GOES) increased due to their consistent pass over rates and large swaths which can easily match temporally to active fires. MODIS is one of the most important and most used because of its approximate 500K saturation in its MIR band (Peterson et al. 2013) with the latest collection (Collection 6) using an integrated approach for its FRP retrieval (Giglio et al. 2016). In application to fire behavior, FRP can estimate fire intensity by calculating the amount of vegetation consumed and rate of smoke emissions.

Among the most common FRP retrieval approaches are a bi-spectral method (Dozier 1981, Zhukov et al. 2006, Peterson et al. 2013, Schroeder et al. 2014) and a single-band mid-infrared (MIR) method (Wooster et al. 2003, 2005; Dickinson et al. 2016). The coarser resolution of satellites indicates that a sub-pixel approach is needed because of major errors in a satellite's point spread function when estimating brightness temperature, especially from lower intensity or weak signal fires (Dickinson et al. 2016). Dozier (1981) developed a bi-spectral sub-pixel approach applied to the Television and Infra-Red Observation Satellite -N (TIROS-N) satellite series infrared bands of the Advanced Very High Resolution Radiometer (VHRR) aboard the NOAA-6 satellite for measuring sea surface temperature, deemed the "Dozier" method. The bi-spectral approach uses both the mid and long-wave infrared bands to allow discrimination of unwanted reflectance characteristics. A sub-pixel approach allows for distinguishment between radiant temperatures of two temperature fields in a pixel at sub-pixel resolution.

Several advancements to the Dozier retrieval have been undertaken including the higher resolution sensor Bi-Spectral Infrared Detection (BIRD) satellite (Zhukov et al. 2006) where pixel clustering was applied to the fire detection algorithm during prescribed fires and estimates of FRP were effectively calculated to within ±30% for 75% of fires. Peterson et al. (2013) improved the FRP sub-pixel retrieval using the bi-spectral method by calculating the FRP over the fire area (FRP_f) instead of the pixel area (FRP_p) where large and small fires with different intensities can be distinguished. Airborne infrared data measured by the Autonomous Modular Sensor (AMS) was compared to MODIS (collection 5) measurements of FRP and found to be highly variable unless errors in MODIS fire detection were corrected.

A relationship and diagnosis of the errors are given in part two of the paper series by Peterson and Wang (2013).

While using a bi-spectral approach, Schroeder et al. (2014) found a strong correlation among ground and airborne sensor fire retrieval data (<1% peak radiant heat flux error), where correlation between airborne and spaceborne FRP measurements was variable (26% in some cases and 10% after error corrections in other scenarios). The weak relationship between airborne and spaceborne sensors is in part because satellites may contain larger amounts of error in FRP estimates due to smoke and cloud cover or pixel point spread functions.

The bi-spectral method may contain errors from either poor co-registration or different atmospheric attenuations between multiple bands, so a physical single-band radiance method that isolates a fire's signal in the MIR region was established (Wooster et al. 2003, 2005). The MIR method was developed based on a pixel's spectral radiance instead of brightness temperature for calculating the FRE from FRP and was used in comparisons between MODIS (single-band approach) and BIRD (bi-spectral approach). Wooster et al. (2003) found values of FRE to be within 15% between MODIS and BIRD of near-simultaneously collected fires in Sydney, Australia of January 2002. A sensitivity analysis for the method is found in Wooster et al. (2005) where the MIR radiance method was validated using ground sensors. An in-depth synthesis of knowledge for satellite retrieval methods of FRP can be found in Wooster et al. (2021).

Field research campaigns have been designed for the extensive capture of wildland fire data while utilizing ground and airborne equipment. During FireFlux II (Clements et al.

2014, 2019) infrared cameras were mounted on towers and a helicopter providing detailed capture of the fire spread with simultaneous measurements of fire-atmosphere interactions. The RxCADRE (Prescribed Fire Combustion and Atmospheric Dynamics Research Experiment) 2011 and 2012 campaigns are one of the most comprehensive wildland fire data acquisition research expeditions to date. Small plots (<1 ha) to large blocks (>100ha) at the landscape scale were burned including both forested and non-forested landscapes, and several remote sensing research teams present their findings. Patterns of fire spread were examined by nadir and oblique ground LWIR sensors using the Stefan-Boltzmann law to estimate FRP and assess fire behavior (O'Brien et al. 2016). Patterns of fuel consumption were examined using ground LWIR sensors and the Wildfire Airborne Sensor Program (WASP) LWIR sensor to derive fire radiative power/energy density (FRPD/FRED) (Hudak et al. 2016). Dickinson et al. (2016) assessed measurement strengths and weaknesses of FRP using ground and RPAS sensors for small plots, and airborne (WASP) and spaceborne (MODIS and VIIRS) sensors for large blocks (Dickinson et al. 2016).

O'Brien et al. (2016) found similar trends in FRP between the nadir and oblique views with the oblique camera measuring slightly higher values, reflecting the heterogeneity in detailed fireline intensity and geometry. In Hudak et al. (2016) temporal resolution of the airborne data was low and FRED was underpredicted compared to ground observations. However, the predicted FRED and fuel consumption observations across sensor types corroborated the 1:1 relationship between FRE and biomass combusted. Due to low experimental replication Dickinson et al. (2016) remark little can be said about precision, accuracy, and bias in their evaluation. Comparisons of FRP between ground sensors and

RPAS were highly variable and comparisons between other sensors were also found to be variable.

It is worth noting that some sources of error in the collection of fire retrieval data and estimating FRP are not a function of the platform (ground, airborne, satellite) used, but rather a function of the sensor or method used (radiance, MIR, bi-spectral, etc.). This might include oversaturation of a sensor in a particular wavelength, choosing a bandpass affected by reflected solar radiation or emittance of hot gasses, poor co-registration between multiple sensors, and making blackbody/graybody emissivity (effectiveness of a body to emit thermal radiation) assumptions. For example, Dickinson et al. (2016) found little correlation between ground, RPAS, airborne, and satellite sensors with errors in calculating FRP mostly due to sensor properties.

Attempts at calculating fire ROS, either by a semi-automated fireline detection algorithm (Paugam et al. 2013) or fully automated active fire edge detection algorithm (Valero et al. 2018), and fireline intensity determined from ROS and FRP (Johnston et al. 2017) have been constructed. Brightness temperature and radiance estimate the arrival time of a fire front at a pixel, denoted as when the brightness temperature of the pixel exceeds 600k (Paugam et al. 2013) or 773k (Johnston et al. 2017), then at a time during fire propagation pixels that identify the fire front are used to calculate ROS. This method was validated by Paugam et al. (2013) during laboratory experiments. Ononye et al. (2007) used differences between burned and unburned areas from multispectral airborne sensors by utilizing the Normalized Difference Vegetation Index (NDVI) and Normalized Difference Burn Ratio (NDBR) to calculate ROS, automatically extracting fireline characteristics.

Paugam et al. (2013) applied the method to bi-spectral infrared sensors aboard a helicopter during a prescribed burn and successfully estimated ROS for more than half of the sensor pixels during the fire. FRP was also calculated and there was little to no correlation between ROS and FRE. Johnston et al. (2017) compared several different FRP methods to calculate fire intensity from only remotely sensed data using the MIR radiance method. It was found that the fire radiative energy density-rate of spread (FRED-ROS) method performed more significantly compared to the other methods and that ROS was successfully calculated from the high resolution (0.13m) sensors. Fireline intensity (ROS) fully described fire perimeter behavior. Valero et al. (2018) applied the canny edge detector operator to a fully automated active fire edge detection algorithm in thermal images that was successfully tested over a range of laboratory and experimental burns. The canny edge detection algorithm was first validated by manual mapping of fire fronts, then applied to the real-time automated algorithm. After an active fire perimeter was established, fire advance to the normal of the fireline was used to calculate ROS.

1.4 Conclusion

A consistent theme within the literature is that high-resolution airborne infrared data is needed to both validate spaceborne sensor measurements and provide data capable of being used for fire behavior modeling. Airborne sensors are often used as means to verify spaceborne measurements by comparison (Peterson et al. 2013, Schroeder et al. 2014, Dickinson et al. 2016) yet can provide higher resolution data usable to infer key aspects of fire behavior (Radke et al. 2000, Riggan et al. 2004), such as fireline intensity and ROS (Paugam et al. 2013, Valero et al. 2018, Wooster et al. 2021), that spaceborne measurements cannot. Experimental and laboratory burns provide valuable information into the intricacies of fire behavior, but often do not burn under the same conditions that wildfires do. This suggests that in order to improve fire behavior analysis, more observations need to be acquired during landscape scale wildfires under changing environmental conditions.

Chapter 2

Automated Extraction of Active Fire Edges From Tactical Infrared Observations of Wildfire

2.1 Abstract

Remote sensing of wildland fires has become an integral part of fire science due to its multiple applications, such as monitoring active fires, evaluating fire effects, estimating fire emissions, and assessing fire risks. Airborne sensors provide high spatial resolution and can provide high temporal resolution enabling fire behavior monitoring at fine scales. Fire agencies frequently use airborne long-wave infrared (LWIR) imagery for fire monitoring and to aid in operational tactics and decision-making. While fire tactical remote sensing systems carry distinctions from scientific instruments, operational support data has the capacity to aid scientific research and fire behavior modeling efforts. However, the potential of this data for scientific use requires specialized data processing pipelines that are not presently accessible. In this work is presented an automated thresholding algorithm coupled with edge detection that delineates active fire edges and is applied to georeferenced LWIR image mosaics. Several automated thresholding and edge detection methodologies were investigated. The proposed method, thresholding around the mean pixel intensity plus canny edge detection, outperformed the other three algorithms, successfully extracting active fire edges over a wide range of image complexity, and was then compared to manually annotated mosaics to compute five performance metrics. The algorithm was tested on tactical LWIR imagery acquired during several fires in California in 2020: the Oak fire in Mendocino County, the Glass fire in Napa and Sonoma Counties, the Slater fire in Siskiyou County, California and Josephine County,

Oregon, and the Creek fire in Fresno and Madera County. These satisfactory results contribute to the integration of infrared fire observations captured during firefighting operations into the scientific research of fire spread analysis and advancement of fine-scale fire behavior modeling.

2.2 Introduction

Recent changes in wildland fire conditions and behavior have brought on new challenges in analyzing and modeling their dynamics. Evolution of extreme fire behavior attributes such as fire spread and intensity (Duane et al. 2021, Hantson et al. 2022) are further leading to unsafe conditions for firefighting operations and the public interface, accentuating the need for accurate fire behavior predictions. The fire spread component is at the foundation of fire behavior models, and the ability to improve model performance is a function of the data that is available.

Remote sensing of wildland fires has become an integral part of fire science due to its multiple applications, such as monitoring active fires, evaluating fire effects, estimating fire emissions, and assessing fire risks. Methods of calculating fire spread with ground devices and ground thermal sensors (Stephens et al. 2008, Rudz et al. 2009) provide ground truth measurements during laboratory and prescribed fire, while visual and infrared remote sensing camera systems provide continuous capture of a fire and a more flexible means of measuring fire spread when placement of ground devices may not be convenient or accessible. Airborne sensors provide a higher spatial resolution and can provide higher temporal resolution than spaceborne sensors, thus enabling fire behavior monitoring at finer scales. Therefore, airborne remote sensing data of fire behavior is of the utmost importance to improve the understanding of extreme fire behavior and support the development and validation of fire behavior models.

Advanced techniques delineate fire spread from camera imagery by means of image processing using feature extraction or image segmentation. Several attempts to find effective ways of identifying fire vs non-fire pixels in visual images during laboratory and prescribed fires use color spacing segmentation with traditional and machine learning methods (Rudz et al. 2013, Toulouse et al. 2016). While segmenting fire pixels in the visual spectrum is useful under clear conditions, background pixels similar enough in color to fire and the presence of smoke can both obscure differentiating between fire vs non-fire pixels and fire edges.

Infrared radiation offers the advantage of having higher transmissivity through smoke and researchers have taken advantage of this by utilizing the mid-wave (Wooster et al. 2013) and long-wave infrared (O'Brien et al. 2016) spectrums to evaluate fire radiative power (FRP) and rate of spread (ROS) (Wooster et al. 2005, Riggan and Tissel 2009, Paugam et al. 2013, Stow et al. 2014). Fire spread has been analyzed from spaceborne sensors such as the Moderate Resolution Infrared Sensor (MODIS, Loboda and Csiszar 2007) and Landsat Thematic Mapper (LTM, Viedma et al. 2015). The consistent availability of spaceborne sensors makes them useful in pre- and post-fire monitoring, however their low temporal resolution and susceptibility to smoke interference make them less suitable for measuring fine-scale fire progression. Furthermore, the low spatial and temporal resolution of spaceborne sensors makes them inadequate for performing and analyzing real-time rate of spread calculations applied to active fire edges needed for operational fire behavior forecasting.

Temperature thresholding used in laboratory or field experiments is an efficient segmentation method, where a threshold is applied to pixel brightness temperature (Pastor et al. 2006, Martinez-de Dios et al. 2011, Paugam et al. 2013, Johnston et al. 2017). Fire front arrival time is designated as the time when these thresholds are exceeded for the first time, and ROS is calculated from the distance traveled. Automated edge detection thresholding techniques were developed for fire imagery by Ononye et al. (2007) and Valero et al. (2017, 2018). Ononye et al. (2007) used the Normalized Difference Vegetation Index (NDVI) and Normalized Difference Burn Ratio (NDBR) from images captured by airborne multispectral and hyperspectral sensors during wildfires. Valero et al. (2017, 2018) used canny edge detection to distinguish the active fire edges with real-time processing in laboratory and field experiments. In other studies, fire fronts and perimeters were manually delineated in Geographic Information System (GIS) from landscape scale wildfires (Stow et al. 2014, 2019, Schag et al. 2021) to capture fine-scale wildfire perimeter progression.

Currently, the extraction of fire pixels, fronts, and perimeters from infrared images takes advantage of image characteristics such as temperatures with an underrepresentation of analysis at the landscape scale. Methods used to delineate fire spread at the landscape scale, either utilized a combination of hyper and multispectral sensors not reasonable for generalized use or manually delineated fire front progression. While these methods have great use and yield satisfactory results, they are inefficient for working with large datasets and specialty equipment is not reasonable to deploy during operational fire monitoring. Except for Valero et al. (2018) where the algorithm was applied to 6600 frames in different scenarios, other techniques have not been as extensively tested.

Fire agencies frequently use airborne LWIR imagery for fire monitoring and to aid in operational tactics and decision-making. This source of data, if managed and processed properly, can be a significant addition to research data collected during small to medium-scale fire field experiments such as FireFlux II (Clements et al. 2014) and the Prescribed Fire Combustion and Atmospheric Dynamics Research Experiment (RxCADRE, Dickinson et al. 2016, Hudak et al. 2016). However, the imaging systems deployed during fire emergencies for tactical decision support are often non-radiometric, which hinders the retrieval of fire behavior metrics. Furthermore, the non-uniformity of landscape scale fires creates challenges in the image processing workflow, for example when setting threshold parameters, which are aggravated by disparities in the imaging sensor or the conditions they are deployed under.

In this work is presented an automated thresholding algorithm coupled with edge detection that delineates active fire edges at the landscape scale and is applied to georeferenced LWIR frames. The algorithm was tested on tactical LWIR imagery acquired on multiple fires in California in 2020: the Oak fire in Mendocino County, the Glass fire in Napa and Sonoma Counties, the Slater fire in Siskiyou County, California and Josephine County, Oregon, and the Creek fire in Fresno and Madera County. Images portrayed fire activity of various intensities and geometries. This analysis seeks to establish the capability to identify active fire progression using basic thermal images by singular means of gradient thresholding not dependent on temperature or other fire characteristics. Successful implementation of these methods can then later be used to calculate ROS. While there are many ways to utilize image processing techniques, several common thresholding and edge detection methods will be discussed, along with the tailored method that produced the best results. Common thresholding and edge detection techniques are investigated in an attempt to keep the active fire edge algorithm as simple and practical as possible while taking processing time into consideration. More advanced techniques may not be appropriate if this processing is to be performed over very large datasets or for operational purposes.

2.3 Background

2.3.1 Thresholding and edge detection

Thresholding is a standard method of image segmentation and a way of converting images into binary form by isolating features in an image. Conversely, edge detection techniques are capable of extracting image object contours. These approaches are advantageous when working with non-temperature-dependent images.

Valero et al. (2018) found canny edge detection to perform significantly better than other gradient masks and edge detection methods at identifying only the active fire fronts, so that method was further explored in this study. Canny edge detector (Canny 1986) first applies a Gaussian filter to smooth the image, detects main edges and discards non-edges, then uses upper and lower thresholding values to identify strong edges and weak edges. Strong edges are considered values above the upper thresholding value and weak edges are considered when they lie between the upper and lower thresholds and are connected to strong edges. Values below the lower threshold are discarded.

OTSU’s method of binarization (Otsu 1979) is a common segmentation method that analyzes an image’s histogram by minimization of weighted variance to obtain a threshold. Pixel values above that threshold are given one value and pixel values below the threshold are given another (0 and 1 for example). Essentially, OTSU’s method identifies two clearly expressed pixel intensity peaks in the histogram and separates the image into two clusters based on the determined threshold value. Multi-thresholding (Huang et al. 2011) allows for the identification of multiple threshold values to classify more than two clusters of pixel intensity into brightness regions (Arora et al. 2008).

2.3.2 Morphological functions

In complex images thresholding and edge detection may exclude pixels required to depict the full object, include pixels outside the wanted perimeter, and may result in broken or non-continuous edges. This can happen when pixel intensities are similar to those of background pixels. Morphological operators are useful ways of dealing with these discrepancies (Ononye et al. 2007) by providing attribute outputs of active elements inside an image. The erosion operation erodes the outer surface of the foreground object (the fire area) where the eroded boundary is turned to zero and white noise is discarded. Dilation increases the size of the foreground object increasing the size of the object area. Since erosion and dilation are often performed together in image analysis, a closing feature utilizes both transformations by first applying the dilation operation and then the erosion operation. Filling binary holes is a transformation based on dilation where background pixels of a binary image inside an identified area are connected and changed to foreground pixels until the boundary is reached. Morphological operators can iterate as many times as necessary. Mathematics and detailed descriptors of morphology can be found in Gonzalez and Woods (2002).

2.3.3 Structure analysis

Detecting edges in complex images often results in more than one identified edge. For instance, some of the images available for this study do not have a distinguished flaming zone such as the one that can be observed in laboratory or prescribed burns where only one or two strong gradients between fire pixels and non-fire pixels exist. Instead, multiple strong gradients may exist inside the fire area making it difficult to outline only a single fire edge. This requires unwanted edges to be removed. Structural analysis and shape descriptors compute connected components of an image, assign a label, and produce statistics for each label. Statistics produced for each component are then used to eliminate edges of certain lengths.

2.4 Methods

2.4.1. Remote sensing data

Tactical LWIR imagery throughout the 2020 fire year in California was requested by the California state fire agency Cal Fire to aid in wildfire management operational decisions, where the data was acquired by various vendors and logged into a database. Features such as fire perimeters, heat sources, and aircraft orientation were also stored with the LWIR imagery for most of the associated flights taken. The 2020 fire season was one of the most intense fire years California has faced with over 4.3 million acres burned, 11 thousand structures destroyed, and 30 confirmed losses of life recorded by Cal Fire 2020 (https://www.fire.ca.gov/incidents/2020/). Within the database, 59 fires were identified representing fires of various intensities in varying topography and vegetation, including data from some of the most significant fires: August Complex, North Complex, CZU Complex, Glass, Creek, SQF Complex, and Apple fires. Images recorded during the fires were 16-bit non-radiometric thermal infrared, with a spatial resolution of 640x512 pixels. Images were converted to 8-bit type before processing to accommodate the input requirements of some existing image processing libraries.

Several fires from the database were selected for analysis. These included the Glass fire, Oak fire, Creek fire, and Slater fire, and were selected based on either request from Cal Fire, or fires where high temporal resolution observations were available. In constructing the active fire edge contouring method, images from six flights during the Glass fire and five flights during the Oak fire were used as they provide a good representation of image diversity. To build the algorithm, images from individual flights were separated for each fire, and images where fire was not present were discarded. Based on visual perception and histogram inspection other images meeting the following criteria were also discarded: images where fire pixels permeated the entire frame as not to have any front or perimeter edge, images scarce in fire pixels where fire geometry was unable to be distinguished, or images that did not contain enough pixels with intensities above background pixels. Examples of images used from the database can be seen in Figure 1. Three Oak fire flights, one Slater fire flight, and one Creek fire flight were used in assessing the automated method performance.

2.4.2 Thresholding and edge detection processing

Identifying fire pixels and the fire area is challenging because the range of pixel intensities and fire geometry can be highly variable from flight to flight and fire to fire. Low-intensity fire pixel values can be proximal to background pixel intensities and clearly defined maximum intensities are not always present. Furthermore, background pixels of the same intensity can reside both inside and outside of the fire area. Therefore, the fire area is defined as an area that contains either a group of fire pixels or a mixture of fire and background pixels if a cluster of background pixels is within the fire geometry. When segmenting images into the active fire area to be edged, thresholding parameters are set to meet this definition distinguishing between the fire area and non-fire area. This definition allows the automated algorithms to be evaluated consistently across all images. Smaller clusters of fire pixels outside the main fire area are also targeted as they may relate to spotting activity. Active fire edges are considered the perimeter of the main fire area and stand-alone clusters (possible spotting) in each frame.

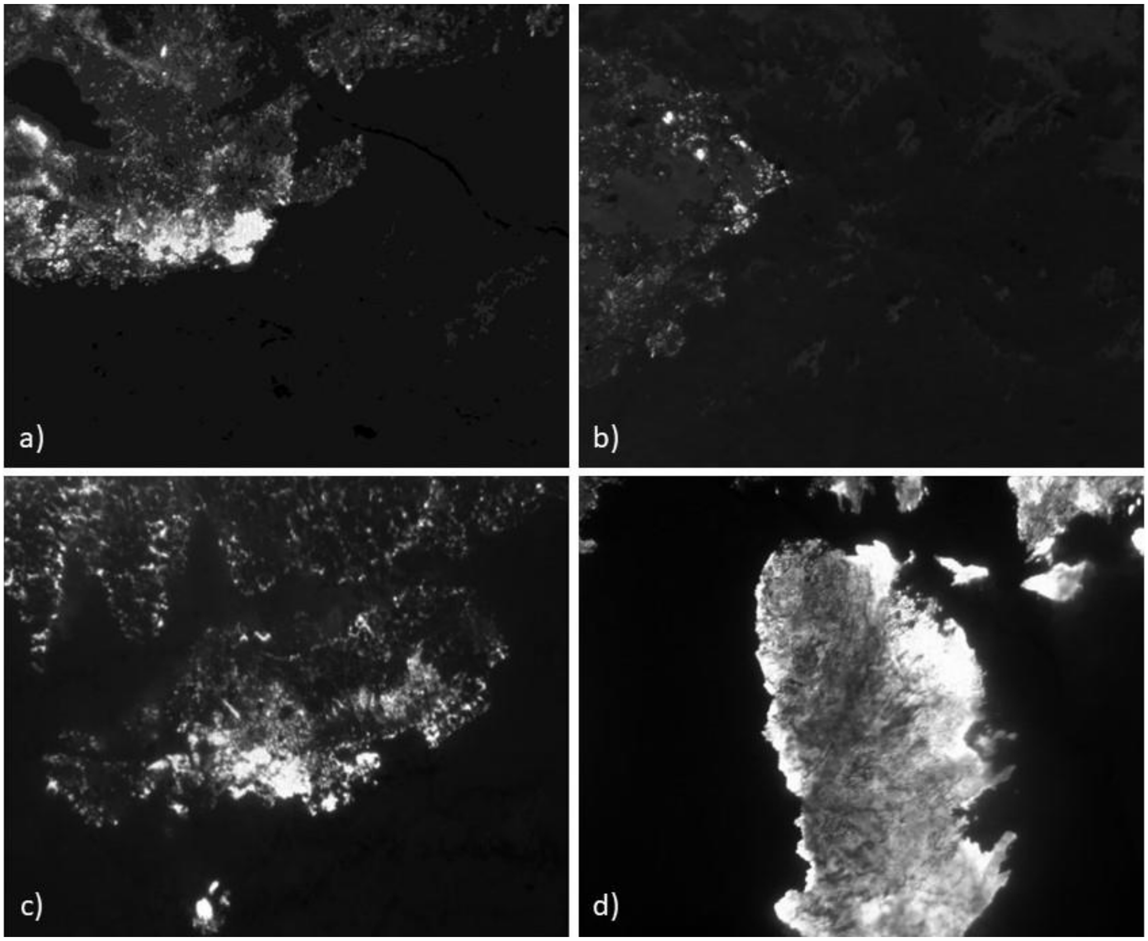

Figure 1. Four LWIR images captured during the 2020 Oak (a, b, c) and Glass (d) fires in California, USA. Pixels that are darker are lower in intensity representative of background values and lower intensity fire, whereas pixels that are white are of higher intensity representative of more intense areas of the fire. These images provide a good representation of how the fire geometries and fire area intensities can vary by image.

Several automated thresholding and edge detection methodologies were investigated. Four combined methods, as described in sections 2.3.2.1, 2.3.2.2, 2.3.2.3, and 2.3.2.4, were constructed using the canny edge detector, OTSU's binarization, and thresholding about the mean pixel intensity. Each image and frame were processed individually.

Unless otherwise stated, a Gaussian filter is first applied before thresholding and edge detection for smoothing and noise reduction using a 3x3 matrix and a standard deviation determined by the matrix kernel. In this instance, the filter takes the kernel size (ksize) in the X direction and the Y direction, and computes the standard deviation (sigma) for each X and Y as,

$$sigma = 0.3 * \big((ksize - 1) * 0.5 - 1\big) + 0.8 \qquad (6)$$

2.4.2.1 Canny edge detector

When only applying the canny edge detector to images, variations of lower and upper thresholding values were tested until two precise values of 3 and 7 were determined to provide the best results. Threshold values higher and lower than the selected values excluded pixels considered to belong to the active fire edge, or extensively over-edged fire pixels including pixels belonging to the background. The size of the Sobel kernel used to find the image gradients in the canny operator was set to 3. A closing operation was then performed with a 5x5 matrix followed by a binary filling operation to connect non-continuous edges. The canny edge detector was then reapplied a second time after the closing operation with different lower and upper threshold values of 0.3 and 0.7. Edge components under 200 pixels in size were removed using connected component statistics to provide only the active fire edge.

2.4.2.2 OTSU's binarization followed by Canny edge detector

Upon inspection of various image histograms and their intensity peaks, OTSU's method was applied in three ways to deal with the heterogeneity and inconsistencies of the histograms. First OTSU's thresholding was applied without any manipulation to the histogram, the second variation applied histogram equalizing and then OTSU's binarization, and the third variation applied histogram stretching followed by OTSU's binarization. After OTSU thresholding the canny edge detector was applied to characterize the active fire edge. Upper and lower thresholding values used in the canny operator were found to hold any value ≤ 4.4 where the lower threshold value is less than the upper threshold value. Connected component stats were used to remove unwanted edges smaller than 200 pixels. It was found that while histogram stretching and equalization improved the performance of OTSU's method in some images, it declined performance in other images and, therefore did not enhance the overall results. Because of this, the analysis was carried out using OTSU's method without any histogram manipulation.

2.4.2.3 Multi-thresholding followed by Canny edge detector

Marginal differences between low-intensity fire pixels and background pixels, and distinguishing between which background pixels to include in the fire area is a challenge when only a single threshold value is applied. Therefore, multi-thresholding based on OTSU statistics may be a more robust method. This would allow for classifying different pixel clusters as background pixels, low-intensity pixels, medium-intensity pixels, and high-intensity pixels to be characterized. The thought behind this approach is that if pixel values could be segmented into multiple clusters of varying intensities, then values could be separated into background pixels that should be included in the fire area and those that should not, pixels of lower fire intensity, and pixels of higher fire intensity. Groups of clusters can then be merged to provide a more complete fire area. A multi-OTSU thresholding operation was performed with four and five classes. Each class was then identified as a single region, and regions containing the wanted clusters of pixels were combined. Canny edge detection was then used with the same structure as when applying OTSU's method. Unwanted edges under 125 pixels in size were removed.

Thresholding by four classes segmented pixel values into two sets of background pixels and two sets of fire pixels, essentially providing a set of background pixels and a set of fire pixels. This fails to provide a classification for those pixel intensities on the border of being background or fire, therefore it was determined that five classes were necessary to achieve the desired outcome. However, the processing time of segmenting a single image significantly increased from minutes to greater than an hour when expanding from four classes to five classes deeming the five-class method impractical for processing large datasets, so the method was carried out using four classes.

2.4.2.4 Alternate intensity thresholding

Here is introduced the fourth proposed method, which combines an automated thresholding method with canny edge detection. Following a visual analysis of 21 diverse image histograms from separate flights and fires, two attempts were made at identifying a threshold using intensity values:

$$TH_p = min_p + max_p * b \qquad (7)$$

$$TH_p = \frac{\sum p_{values}}{n_{pixels}} * b \qquad (8)$$

where TH_P is the threshold value, min_P and max_P are the minimum and maximum pixel values in each image, p_{values} are the pixel values, n_{pixels} is the number of pixels in an image, and b is a parameter. Of Eq. (7) and Eq. (8), Eq. (8) produced the best results so it was selected for analysis. Different values of b were investigated until the highest performance value of b=1.015 was selected based on visual inspection.

From the Gaussian smoothed image, the threshold mask was applied. Two filling functions were used to fill the fire area followed by two iterations of dilation and another filling operation. This ensures there is only a single edge inside the fire area when edge detection is applied, otherwise multiple edges may be detected. Erosion was then applied to reduce any part of the fire area that protruded from the perimeter or any rogue non-fire pixels scattered throughout the frame. Dilation and erosion transformations were done using a 5x5 matrix. Even though dilation was followed by erosion, the closing morphological function was not applied here because two iterations of dilation were necessary but only one iteration of erosion was necessary. Finally, canny edge detection was performed with an upper threshold value of 4.4 and a lower threshold of any value <4.4. Edges smaller than 250 pixels were removed. Figure 2 illustrates results after each principal process is applied when utilizing sequentially a threshold mask from equation (8), morphological operators, and then canny edge detection. It can be seen in Figure 2b that morphological operations are necessary to transition from discrete active fire edges around the fire area to a continuous edge more adequate for running edge detection. The final output image provides a sharp continuous line around the active fire edge. Figure 3 shows a block diagram outlining the various processes used in the four methods for identifying the fire area and active fire fronts.

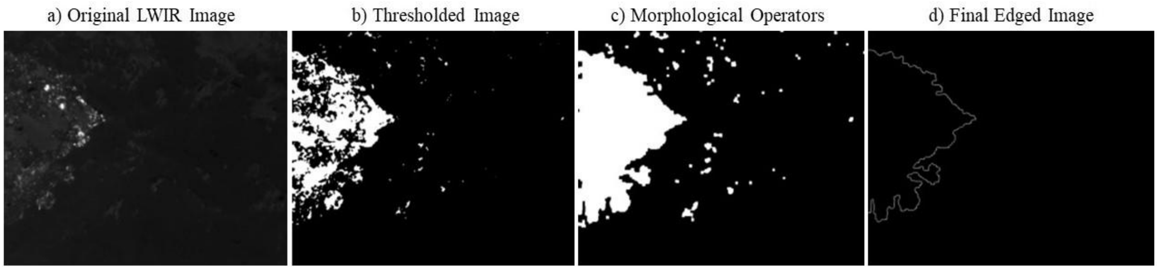

Figure 2. Progression of the processes involved in contouring active fire edges. a) is the original LWIR image, b) is the output of applying the threshold mask utilizing equation (8), c) is an output of the threshold mask after applying morphological operations, and d) displays the final output when applying the canny edge detector and removing unwanted edges. b) provides a good example of why morphological operations are necessary after applying a threshold mask given the gaps along the edge of the fire area. Looking at c), gaps in the active fire edge and area have diminished leaving a more continuous edge to be contoured.

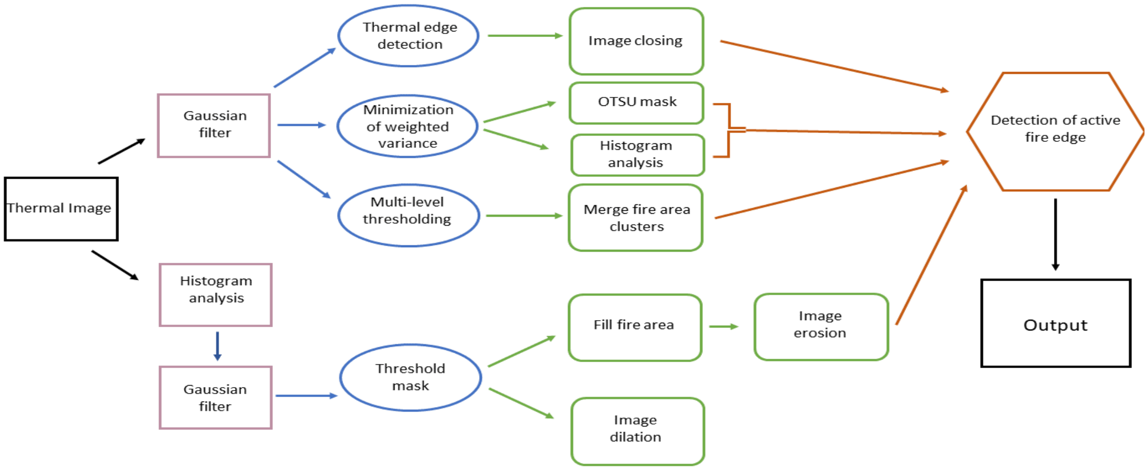

Figure 3. Block diagram showing the order of operations for the four automated methods tested (canny edge detection, OTSU's binarization, multi-thresholding, and thresholding about the mean pixel intensity). Black boxes are the input and output, purple boxes represent the initial step for each method, blue ovals are the main thresholding or edge detection algorithm used, green soft rectangles are secondary analysis tools such as morphological operators, and the orange hectogon signifies the final step of detecting the active fire edge.

2.4.3 Polygon functions

Each group of raster edge pixels was translated into polygons by utilizing the polygonize function. By translating the edged pixels into polygons comparisons can then be made between the automated polygon and ground truth polygon. Due to transformations between raster types and polygons, not all active fire edges were converted to be continuous, therefore dilation was necessary. In more complex mosaics, only applying the polygonize function and dilation was insufficient because the fire edge still lacked continuity, unable to render a single polygon. Instead, an alpha shape function (a concave geometry enclosing vertices) was used to produce a continuous polygon. An alpha value of 0.015 was applied and holes created by the concave hull within the edge polygon were eliminated. For Oak Flight 3, several minuscule holes persisted in the polygon and therefore were closed manually without any new digitization. It is worth noting the extra processes used are a result of working with raster images and not a function of the automated algorithm. The use of the polygonize function and alpha shapes allows for the creation of single polygons of the edged mosaics in order to assess error metrics in the automated method. Manually annotated vertices were drawn around the main active fire edge for each of the selected flight mosaics to enclose a single fire area governing as ground truth.

2.5 Results

2.5.1 Automated methods comparison

Applying strictly canny edge detector, OTSU's binarization, and multi-thresholding produced highly variable results, working well in some cases when the fire area and geometry were clearly defined yet failed to produce satisfactory results in more complex images. In some cases, they even failed to produce satisfactory results in simple shapes with a clearly defined fire area. Adjustments to achieve satisfactory results fluctuated between modifications, i.e. while one adjustment worked well for some of the images, detail was either lost or excessive in other images. Results also varied when the methods were applied to images acquired under different flight and atmospheric conditions. In most instances, other image processing operations (such as morphology) would have made no reasonable change in the overall performance of the method. Therefore, it was difficult to achieve input thresholding parameters successfully for the majority of images.

Canny edge detector tended to over-edge images producing unwanted edges belonging to background pixels, not identifying edges belonging to the active fire edge, or excessively edging the fire area. Given the complexity of the images, especially where there is high intermixing of fire and background pixels inside the fire area, this is unsurprising.

Non-homogeneity in image histograms and non-uniformity in histogram peaks posed challenges for the OTSU algorithm to consistently threshold the entire fire area. Images where fire intensity is lower will have two peaks closer together and proximal to the background pixels. Images where there is a larger number of high fire intensity pixels will have a second peak at the maximum value giving a higher degree of separation between the two peaks used to calculate the threshold value. Consequently, only pixels with values belonging to the most intense portions of the fire were thresholded and edged. Overall, OTSU’s method worked well for identifying high-intensity spots of the fire in an image but performed poorly in thresholding the entire fire area within the image and, therefore was ineffective in allowing for the entire active fire edge to be identified.

Multi-thresholding successfully classified the images into four pixel intensity clusters that could be combined into regions of interest and produced better results than single OTSU thresholding. However, the four classes were unable to segment differences between wanted background pixels inside the fire area and unwanted background pixels. Unreasonable processing speeds when using five classes are a function of the OTSU statistics (Arora et al. 2007), and future attempts at multi-thresholding might have success implementing other methods.

Automated thresholding conditional to the mean pixel intensity followed by canny edge detection outperformed the other three algorithms successfully extracting active fire edges over a wide range of image complexity. Not only did the proposed method in this study contour edges along the main fire perimeter in each frame, but it also contoured smaller clusters of fire pixels separated from the main fire area possibly indicative of spotting. Active fire clusters not belonging to the main fire area that were not edged are a result of having to remove edges below a certain size, where they may have originally been outlined, but then discarded when filtering edges out. In a few cases, the algorithm underperformed by capturing edges extending from the fire area, not capturing the full active fire edge, or breaking continuous segments into multiple edges. As expected, these mostly occur where no clear active fire edge is defined, fire pixels are speckled throughout the image, and where there are high mixtures of fire and background pixels.

This method was then selected for implementation on georeferenced images where automated edges are compared to manually annotated edges and performance metrics are computed for several flights. Comparisons between final outputs of segmentation techniques and the original LWIR images can be seen in Figure 4. Each method was manually tailored to provide the best outcome, so the representative images compare the best results. Figure 5 provides an example of how the new method underperformed in contouring the active fire edge.

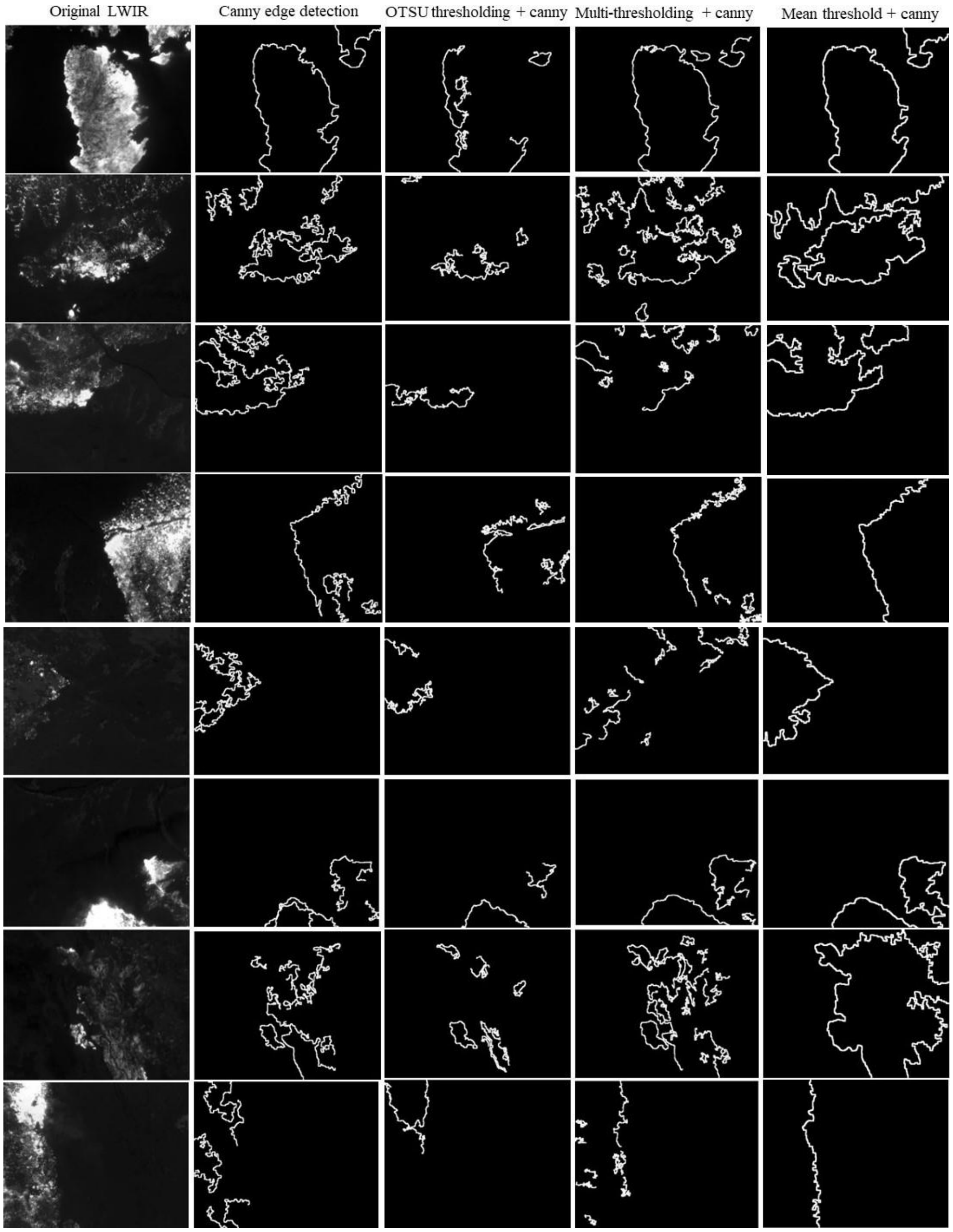

Figure 4. Four methods of extracting active fire edges are compared against each other and to the original LWIR image. There is a clear distinction between the performance of the fourth method compared to the other three. Mean threshold plus canny edge detection is able to capture active fire edges throughout the diverse fire intensities and geometries.

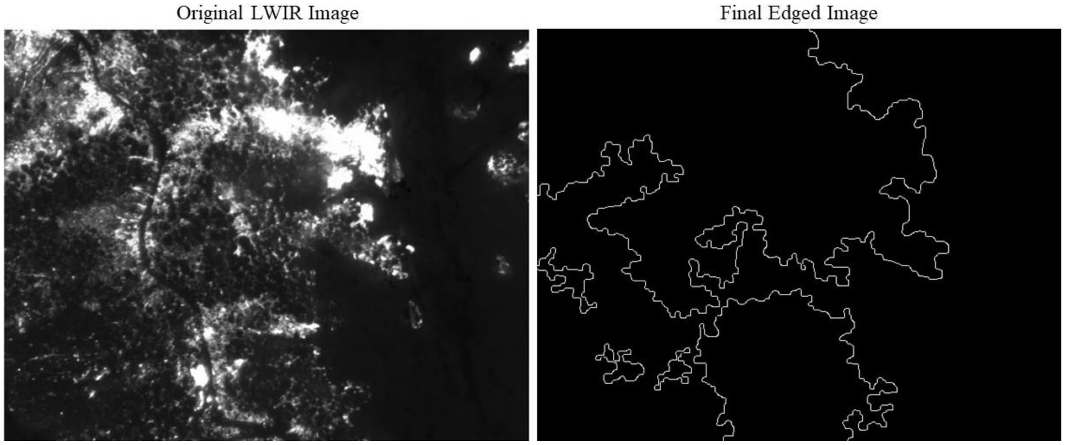
Original LWIR Image

Final Edged Image

Figure 5. The original image (left) captures a distinct active fire edge extending from the top of the frame to the bottom of the frame. After the mean threshold with canny edge detection is applied (right), the method does not delineate the continuous active fire edge in the original image. Rather it follows gaps in the higher-intensity regions.

2.5.2 Application of automated method

The automated algorithm was applied to individual LWIR raster images to produce a binary raster image containing the fire edge and non-fire edge pixels, where they were georeferenced to generate a contoured mosaic of the entire fire edge as seen in Figure 6. Images were pre-filtered by maximum pixel value to create mosaics containing only images with fire. Detailed edges around the active fire perimeter were observed in the binary raster images also capturing spot fires, however, double edging occurred in some areas. Examining Figure 6, the algorithm also identifies a few isolated regions away from the main fire area and a curl extending from the southern aspect of the main fire geometry even though they are characterized as the background. It is hypothesized that double edging is a proponent of inconsistent edging between concatenated images. Even though an active fire edge may be contoured correctly in one image, it may not be correctly contoured in a concatenated image if the corresponding fire area is not fluent in fire pixels. The gdal merge function also prevents overlaps by using data from the last image provided when multiple images overlap, but non-fire edge pixels are interpreted as containing “no data” and did not overlap with edges detected in another image. Classification of background pixels as fire pixels outside the active fire edge is a function of the difficulty in defining a threshold value that distinguishes pixels belonging to the fire area and not belonging to the fire area.

Figure 6. A mosaic of the automated method applied to binary individual georeferenced single flight images during the Oak fire. When applied to individual images the algorithm characterizes more detail in the shape of the active fire edge, but segments the main fire area into multiple fire areas.

The discrepancy in overlapping edges was solved by applying the automated edge algorithm to georeferenced image mosaics as displayed in Figure 7. Mosaics of the original LWIR georeferenced images were created in the open-source GIS platform QGIS for flights of selected fires. Five flights were then selected for evaluation: three flights during the Oak fire, one flight during the Slater fire, and a single flight capturing the Creek fire. Flights were selected based on the continuous structure of the active fire edge which permits a more robust analysis.

Figure 7a provides an example of a single flight georeferenced mosaic during the Oak fire, where a notion of the image complexity and how fire geometry and intermixing of pixel intensities present a challenging structure to work with. Figure 7c displays the performance of the automated algorithm after being applied to the Oak fire flight mosaic, and Figure 7d is the manually delineated active fire edge. By applying the algorithm to mosaics, the spatial reference information is retained. This change in processing order also removed the edges detected within the active fire perimeter (Figure 7b). Several noticeable disparities exist between applying the algorithm to individual images in a flight versus a flight mosaic. When applied to the mosaic, (Figure 7c) the main fire area becomes a single continuous polygon more complementary to the manually annotated mosaic (Figure 7d), whereas applying the method to individual images produces a sharper edge yet neglects faint intensities often cutting inside the fire geometry to follow more distinct intensity gradients. Second, is that when applied to individual georeferenced images the edge is not only sharper around the active fire perimeter but distinguishes between fire and smoke. In Figure 7c on the southeast region of the fire geometry, the contoured line follows a thin layer of smoke that extends from the fire edge increasing the area size.

Two flights from the Oak fire (Oak Flight 1, 2) and one flight from the Slater fire were the only cases where a continuous active fire edge polygon was created without the need of a concave hull tool. The flight from the Creek fire, while representing the most extensive capture of the fire, had gaps in the active fire edge over half a mile in some cases, preventing the creation of a single polygon even when alpha shapes were utilized. Because of these gaps, the Creek fire image was excluded from the evaluation.

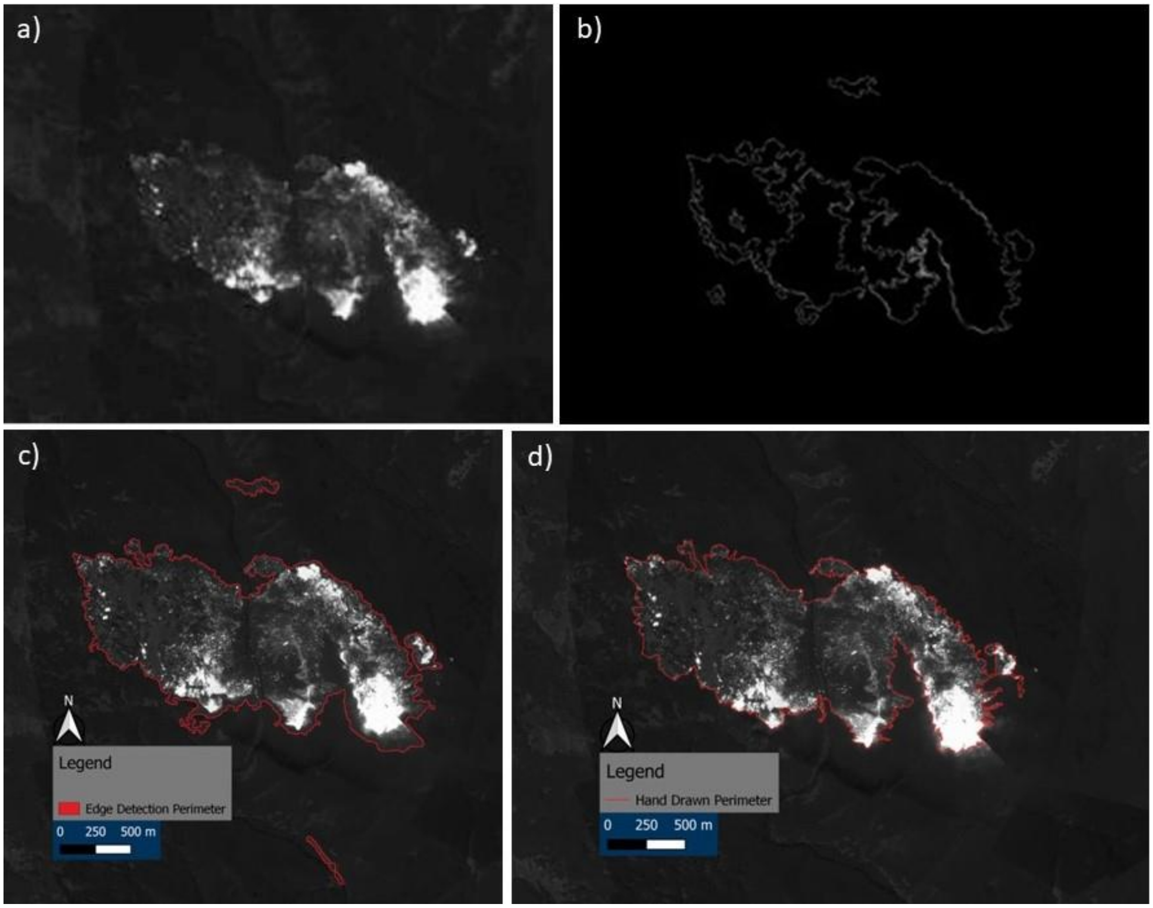

Figure 7. a) Mosaic of a single flight taken during the Oak fire (flight 0533), b) mosaic built after applying the automated algorithm to individual frames, c) result of applying the automated algorithm to a single flight mosaic, and d) mosaic manually annotated active fire edge. When applied to the mosaic (c) a single continuous polygon is created in the main fire area and the double edging is diminished.

Overall, the automated algorithm displayed better performance when applied to flight mosaics instead of individual images, so error metrics were calculated for this process. They were assessed for each of the two georeferencing edged applications: when the delineated active fire edges were polygonized, or when the polygonize function alone was insufficient and polygons were created with the use of concave hull.

2.5.3 Performance Metrics

Five evaluation criteria were used in measuring the performance of the automated algorithm: Figure of Merit (FOM, Pratt 1978) and Baddeley distance (Baddeley 1992) were used to assess the similarity of lines produced by the automated edging method and ground truth digitization, the Jaccard index (Jaccard 1901) used to measure similarity between the intersection and union of the two sets, spatial difference in area to provide a ratio of the automated area to the manually annotated area, and the difference in areas between the automated and manual polygons.

FOM and Baddeley distance are common statistical evaluations that have been found useful in assessing segmentation contouring and in wildfire image performance, and were performed following the methods of Valero et al. (2018) described by Eq. (9) and Eq. (10). FOM characterizes the accuracy of one method against another by inspecting dislocated pixels with a dimensionless output value between 0-1, where a value of 1 is the best achievable value. Baddeley distance is a metric in meters designed to measure the performance between binary images comparing edged or segmented image features with the true image, in this case, the distance between vertices along the automated edge and manually edged image. FOM and Baddeley distance are calculated as:

$$FOM\left(I, I_{gt}\right) = \frac{1}{max\left[card(I), card(I_{gt}\right]} \sum\nolimits_{k \in 1} \frac{1}{1+\alpha \cdot d(k, I_{gt})^2} \tag{9}$$

$$BAD\left(I, I_{gt}\right) = \left[\frac{1}{card(I)+card(I_{gt})} \sum\nolimits_{k \in I \cup I_{gt}} \left|d\left(k, I_{gt}\right) - d(k, I)\right|^P\right]^{\frac{1}{P}} \tag{10}$$

where I is the segmentation result, I_{gt} the corresponding ground truth (hand drawn polygon), card() is the cardinality of the curve, and d(k, I_{gt}) is the minimum distance between point k and curve I_{gt}. $I_{gt} \cdot \alpha$ is a constant 1/9.

The Jaccard index, another common statistical evaluation, was also selected because of its simplicity and universal ability to compare the similarity between two finite sets, and is expressed (Costa 2021):

$$J(A,B) = \frac{|A \cap B|}{|A \cup B|} \qquad (11)$$

where A and B are a polygon set. Jaccard index values range from 0-1 where 1 indicates the two sets are identical. Perimeter differencing provides an opportunity to inspect a non-dimensional normalized difference between the automated active fire edge perimeter and the ground truth annotated perimeter, which can also provide insight as to whether the algorithm more commonly under-edges or over-edges. Perimeter differencing overlayed the automated and manual polygons to calculate the areas where they diverged. Outer differencing is where the automated active fire edge detection overextended the fire edge compared to the manually drawn edge, and inner differencing is where the automated detection contoured the edge inside of the manually drawn perimeter. The area of the automated edge detection polygon falling outside and inside the hand-drawn polygon was divided by the total area of the hand-drawn polygon to produce the outer and inner error, where a value of 0 indicates no difference between the two polygons.

In calculating FOM and Baddeley distance metrics, only the main body of the fire area was taken into consideration, neglecting the smaller false detections by the automated algorithm. For these calculations, we are interested in how accurately the automated polygon was detected compared to a manually annotated polygon. The reason for this is that the FOM and Baddeley metrics are comparing displaced pixels and distances in relation to the manual polygon, so false positives can give unreasonable performance errors, making the values more difficult to interpret. Jaccard index, inner and outer differencing, and area comparisons were all made using both correct and incorrect detections of the fire area. Table 1 includes metric values of the error indices for the statistics calculated in each case of the selected flights.

FOM values were close to zero for both the polygonized and concave hull applications with average values of 0.056 and 0.078. These values imply poor performance by the automated method, however FOM is influenced by the overall size of the polygons, and as far as we know has only been applied to laboratory or experimental fires (Rudz et al. 2009, Valero et al. 2018). When working at the landscape scale with mosaic images, fire areas and polygon size are much larger compromising the performance of FOM as an evaluating metric.

Baddeley distances ranged between 14.32m for Oak Flight 2 and 167,510m for Oak Flight 3, with an average value of 41,906m when using the polygonize function and 36.174m when using the concave hull function. Even though these values are within an expected range, as with FOM the Baddeley distance is also affected by the overall scale of the polygons, so as the scale in size of the polygons increases the Baddeley distance and FOM metrics will naturally increase as well.

Inner and outer difference values were all closer to zero with a maximum value of 0.322 when the polygonize function was used for Oak Flight 3. Average values for the inner and outer difference when mosaics are polygonized are 0.098 and 0.080 with a total (inner plus outer) average difference of 0.179. Average values for the inner and out difference when the concave hull is applied are 0.041 and 0.135 with a total average difference of 0.176. Values for differencing undergo a behavior opposite that of the Baddeley distance in that as the area of the true polygon increases, the inner and outer differences are divided by a larger number so the error will decrease as scale increases. Figure 8 provides an illustration of inner and outer differencing for the flight during the Slater fire (flight 0553). One prominent differencing error in purple (inner difference) can be seen where few fire pixels continue the active perimeter and the automated method cuts inside the fire area, but the majority of differencing errors are minor.

Jaccard index values were all above 0.7 ranging from 0.725 to 0.928. Average Jaccard indexes were similar between the polygonize function 0.832, and the application of the concave hull 0.838. The high Jaccard index values indicate that the regions inside the automated polygon are also mostly inside the manually drawn polygon and the two polygons are very similar.

Simulated burn area is often compared to true burn area in assessing the performance of fire behavior models (Monedero et al. 2019), and when initiating a model run from infrared polygons (Kochanski et al. 2019, 2021) it is important to understand the accuracy of the polygon dimensions. For this, we assess the differences in area by subtracting the area of the automated polygon by that of the ground truth polygon. The largest difference occurred for the Slater flight which underestimated the active fire area by 3,265,051m^2, and the smallest difference was Oak Flight 3 which overestimated the area by 249,116m^2. Concave hull produced the highest difference in area for Oak Flight 1 over-edging the active fire area by 533,939m^2, and the lowest difference in area occurred for Oak Flight 3 under-edging the area by 129,149m^2. Average differences in area when polygonized is approximately 1,058,549m^2, and approximately 332,551m^2 when a concave hull is used.

Table 1. Five evaluation metrics used to assess the performance of the automated method. Baddeley distance, FOM, Inner/Outer difference, Jaccard index, and Area.

Metric	Oak Flight1	Oak Flight2	Oak Flight3	Slater Flight
Concave Hull – Baddeley(m)	43.416	26.718	17.484	57.078
Concave Hull - FOM	0.0132	0.0424	0.2486	0.0086
Concave Hull – Inner Difference	0.0010	0.0015	0.1215	0.0382
Concave Hull – Outer Difference	0.2231	0.2169	0.0666	0.0346
Concave Hull - Jaccard Index	0.7771	0.8206	0.8237	0.9284
Polygonize – Baddeley(m)	24.336	14.322	1.6751e5	78.391
Polygonize - FOM	0.0666	0.1195	2.1128e-8	0.0395
Polygonize – Inner Difference	0.0020	0.0081	0.3223	0.0615
Polygonize – Outer Difference	0.1154	0.1455	0.0377	0.0227
Polygonize – Jaccard Index	0.8176	0.8659	0.7253	0.9177
Area of hand drawn polygon (m^2)	1,869,620	2,280,438	2,352,536	84,022,008
Area of polygonized polygon (m^2)	2,276,263	2,593,825	2,103,420	80,756,957
Area of concave hull (m^2)	2,403,559	2,771,607	2,223,387	84,197,956

Based on visual inspection of Figure 9, where a comparison between the automated edge detection method applied to image mosaics, the concave hull applied to mosaics, and the manual annotations are overlayed, it can be seen that there is general agreement between the automated method and manual annotations of the main fire geometry in Figure 9a,b,d and less agreement in Figure 9c. The automated method visually performed best for the Slater fire flight (Figure 9d). With the use of the polygonize or concave hull, the active fire edge provides a smoother active perimeter compared to the hand-drawn perimeter, but still captures the fire geometry (shape and size). Over areas of higher fire intensity where the gradient is stronger, the automated and manual edges are analogous, but in areas where small fingers of fire extend from the fire area, and areas where smoke is present, have shown to be problematic.

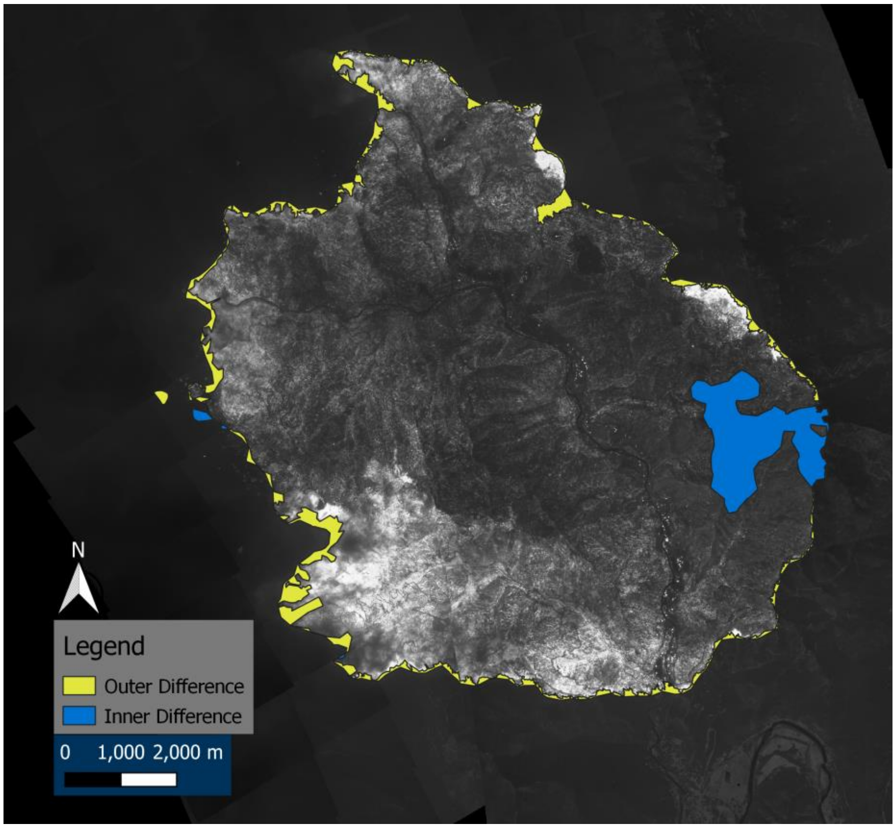

Figure 8. Perimeter area differencing between the automated edged delineation and manual annotation delineation of the active fire edge. Areas shaded in pink are the outer difference between the automated and manual methods, and purple is the inner difference.

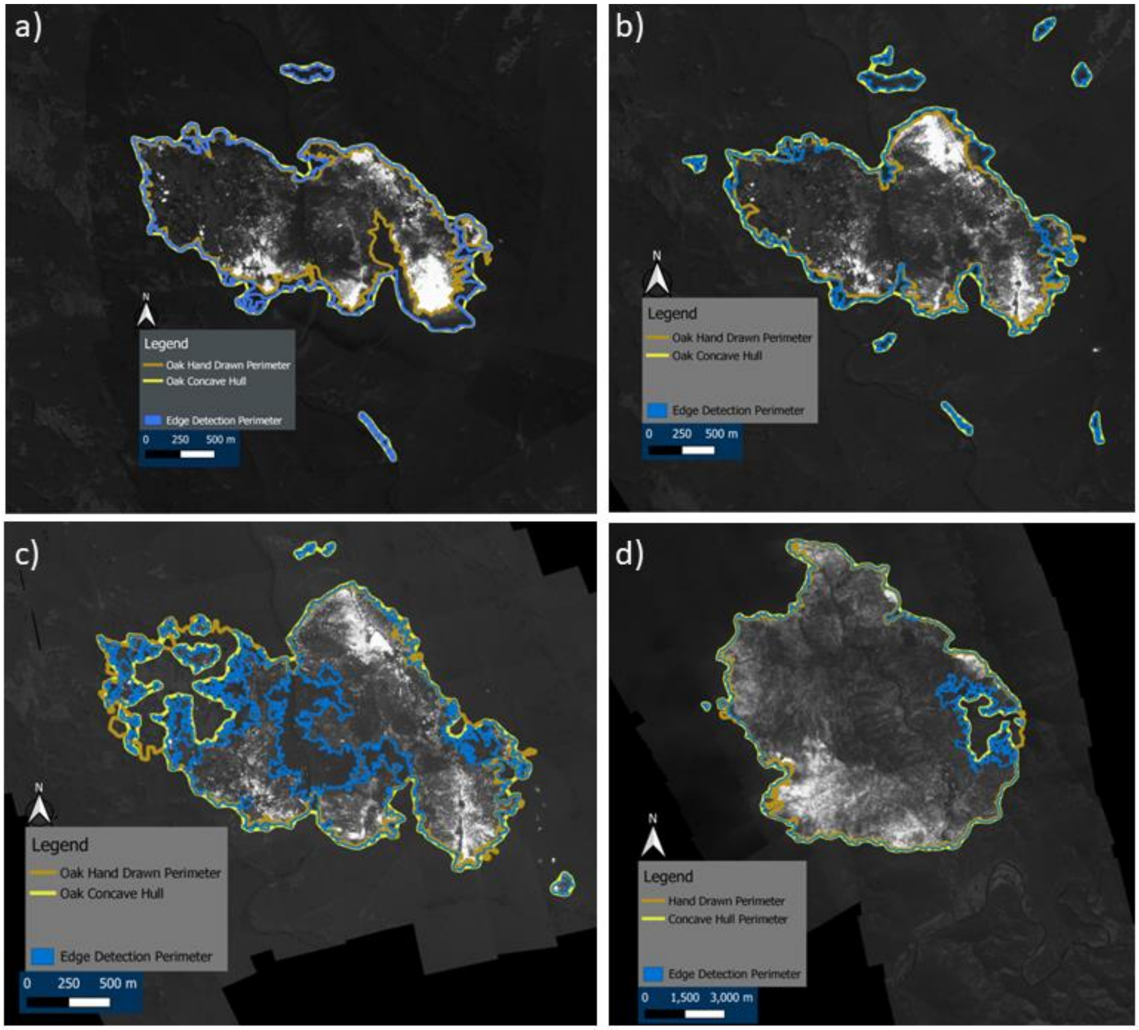

Figure 9. The four flights used in evaluation metrics: a) the Oak fire flight 0533, b) Oak fire flight 0535, c) Oak fire flight 0537, and d) Slater fire flight 0553. Each image provides a visualization of the automated method applications. The blue dotted line represents the results of applying the automated method directly to mosaics, the yellow line is after applying the concave hull, and the brown line is the hand-drawn annotation.

2.6 Discussion and conclusion

Remote sensing techniques used to monitor and observe wildfire is a critical component of understanding fire dynamics. Their versatility provides means of assessing active fire scenarios from various platforms. However, acquiring the needed observations to improve fire spread calculations is challenging. The dataset used here, while lacking radiative components of fire, has an extensive number of images that provide value to develop fire spread forecasting models. Automated methods of image processing for extracting active fire edges were evaluated and compared. A new method proposed in this research, thresholding about the mean pixel intensity plus canny edge detection, outperformed several other common thresholding and edge detection algorithms. The new method provided satisfactory delineation of active fire edges over a range of image complexity belonging to multiple fires. It is worth noting that while this algorithm works well for these case studies, it is likely some parameters will need to be adjusted when working with other fires or datasets. As described in section 3.2 the size of edges that need to be removed will fluctuate depending on which processing method is used and which flight is being processed. Iterations of morphological functions such as dilation and hole filling will also likely need to be adjusted for different fires. Furthermore, setting an automated threshold value may fluctuate for different fires, and small changes in the value of b in equation (8) can produce under or over-thresholding.

Typically, within laboratory and field experiments fire spread takes on more of an elliptical form providing a simpler shape to segment and contour, however the heterogeneous fire geometry at the landscape scale can enhance the difficulty in constructing active fire edge algorithms. Although, should this type of data be used to improve fine-scale fire behavior modeling, it may be acceptable to provide polygons of an active fire edge that do not precisely follow a detailed cut-out of the perimeter, but rather a smoothened version of the polygon like the one provided when applying the concave hull in Figure 9.

While the method appears to perform well in this study, the successful algorithm is dependent on the use of multiple iterations through morphological functions implying that standard thresholding or edge detection techniques alone are not adequate enough to extract active fire edges in complex images. Rather, it is necessary to develop intensive algorithm structures. Some of the result disparities may also be a function of pixel saturation. Sensors capturing high-intensity portions of fire will often saturate which can bias image histograms at the maximum value.

The automated method performed more comparable to ground truth delineations when applied to georeferenced flight mosaics versus georeferenced individual images. Use of the polygonize function and alpha shapes allowed for the creation of single polygons of the edged mosaics to assess error metrics in the automated method by calculating FOM, Baddeley distances, the Jaccard index, a normalized area difference ratio, and differences in polygon areas. FOM values showed poor similarity metrics between the automated and manual method, and while Baddeley distance values were in an expected range, it is important to remember that FOM and Baddeley distance are affected by the overall size of the polygons, and may not be appropriate in landscape scale fire delineation analysis.

These results set a foundation for the use of infrared fire observations captured during firefighting operations in fire spread analysis to be applied for research applications. This allows for the evaluation of higher-resolution fire spread dynamics during bouts of extreme fire behavior at the landscape scale, which will in turn serve to develop and advance fine-scale fire behavior models. Our results also reiterate the need for improved methods of extracting high-resolution active fire perimeters from airborne infrared imagery, such as those at the landscape scale when fire temperature thresholding is not available. As future research campaigns focus on taking infrared measurements during landscape wildfires, enhanced automated methods capable of handling large amounts of data are going to be necessary.

Future work will include improving these image processing methods for landscape scale fires taken from high-quality airborne sensors where fire behavior metrics such as fire radiative power are available. Identifying a threshold capable of identifying background pixels belonging to the fire geometry and those not belonging to the fire geometry will continue to be a difficult task in working with complex fire images of this size.

Chapter 3

Analysis of High-Resolution Airborne Thermal Infrared Fire Behavior Data Collected During the California Fire Dynamics Experiment (CALFIDE)

3.1 Abstract

In-situ measurements of wildfires are increasingly important to meet the objectives of the fire community and provide invaluable data for fire behavior analysis. During the California Fire Dynamics Experiment (CALFIDE) field campaign the San Jose State Wildfire Imaging System (SWIS) aimed at acquiring landscape-scale high-resolution wildfire data, successfully capturing fire behavior during the Mountain and Mosquito fires in California, USA 2022. This study focuses on integrating data from two infrared bandpass cameras with an Inertial Navigation System (INS) to develop advanced processing methods, and facilitate the generation of georeferenced orthomosaics enabling the calculation of fire radiative power (FRP) and a detailed analysis of fire spread. While challenges were encountered with the georeferencing of MWIR images, LWIR imagery was successfully georeferenced to observe fire spread, calculate FRP, and improve the automated active fire edge detection method presented in Chapter 2. This analysis acknowledges the complexities of building sophisticated methods for processing data of this stature, but emphasizes the need for future improvements. The results actively contribute to the advancement of processing techniques for high-resolution wildfire data and open the capability of that data to be used for a more extensive analysis of fire behavior.

3.2 Introduction

Our understanding of fire dynamics has greatly improved with increased research efforts and the development of modern research equipment. However, the knowledge of fire behavior and the ability to accurately forecast that behavior is still lacking, partially due to the inadequate amount of comprehensive research-quality data available. Many laboratory and field experiments have been conducted in an attempt to measure and quantify fire behavior parameters, yet fire behavior models continue to struggle to accurately simulate and forecast fire behavior during landscape scale wildfires consistently. Obtaining the necessary wildfire data is challenging though. The uncertainty in fire ignitions and environmental conditions driving behavior means that resources must be reactionary in their response to fire activity and the equipment used to collect data needs to be of high caliber.

During recent years, there has been increased attention to capturing in-situ fire data during wildfires where remote sensing and ground-based instruments are able to provide a diverse dataset. Airborne infrared (IR) thermography is a critical component of measuring high-resolution fire spread and estimating fire intensity of wildland fires, and the success of evaluating fire behavior is a proponent of the specific wavelengths used to measure the fire, the resolution at which the fire is observed, and the ability of the operating system. Research campaigns utilizing this method of study, such as the Fire Influence on Regional to Global Environment on Air Quality (FIREX-AQ) campaign where aircraft observations were able to help provide a comprehensive analysis of pyroCb activity during the Williams Flats fire in 2019 (Peterson et al. 2022), are gaining importance. Several IR camera sensors have been used in collecting and analyzing wildland fire data such as the Autonomous Modular Sensor (AMS, Peterson et al. 2013, Schroeder et al. 2014), Wildfire Airborne Sensor Program

(WASP, Dickinson et al. 2016), FireMapper 2.0 (Stow et al. 2019), and the MODIS/ASTER Airborne Simulator (MASTER, Peterson et al. 2022). These analyses have provided valuable information about the fire behavior, but are either performed on experimental burns, provide low temporal resolution of the fire, have a limited number of repeat passes over the fire, or are of a lower spatial resolution.

CALFIDE was a collaborative field campaign between NOAA Chemical Sciences Laboratory (CSL), San Jose State University (SJSU), University of Nevada Reno, and NASA Goddard to study wildfire behavior from a NOAA fixed-wing aircraft in coordination with mobile ground sensors. Instruments aboard the aircraft included equipment to measure atmospheric chemistry, a scanning Doppler lidar to survey horizontal wind field and vertical plume dynamics, and the SWIS instrument to provide high-resolution infrared thermography of the fire behavior. Ground-based mobile Doppler radars and lidars were also used to measure wind fields and plume dynamics.

CALFIDE provided an initial attempt to measure and analyze wildfire behavior with the SWIS instrument capable of capturing fine-scale fire behavior with high resolution. During the campaign, SWIS flew over several fires in Oregon and California including Rum Creek, Mountain, and Mosquito. Upon the successful capture of the data, this research analysis focuses on the Mosquito and Mountain fires detailing the methodology performed in processing sensor frames. MWIR and LWIR camera data was processed and matched with data from the INS, the infrared frames were georeferenced, brightness temperatures (BT) were used to calculate FRP, and active fire edges were extracted with an attempt to improve upon the methods in Chapter 2. Explored in this analysis are the robust methods used to integrate data captured by two infrared bands from different cameras, functionality of the camera data, and the ability to use extensive wildfire data for an analysis of fire spread and intensity.

3.3 Methods

3.3.1 Fire observations

SWIS is a state-of-the-art infrared sensor package comprising two radiometric cameras with different thermal band passes and an INS that records camera orientation dimensions and navigation. The MWIR camera is a Telops FAST M150 with a spectral range of 3-5µm and a spatial resolution of 640x512 pixels, that comes with four temperature range filters. The LWIR camera is a Workswell WIRIS Pro with a spectral range of 7.5-13.5µm also capturing at a spatial resolution of 640x512 pixels and is equipped with a visible camera. Frames from the cameras are stored as 16-bit types. Using both IR bands allows for simultaneous capture of peak fire emittance and intensity and the landscape. Brightness temperatures from both sensors can then be used to calculate FRP, and the LWIR images can be used to delineate active fire edges. The setup of the SWIS instrument is displayed in Figure 10.

Figure 10. The NOAA Twin Otter (left), and a display of the SWIS instrument aboard the Twin Otter (right). The instrument points out the bottom of the aircraft providing a nadir view of the fire.

SWIS flew aboard the NOAA Twin Otter providing a nadir viewing angle outside the bottom of the aircraft. The camera system provided a detailed capture of the active fire edge during the Mountain fire in Siskiyou county, California on September 3, 4, and 6, 2022, and the Mosquito fire in El Dorado and Placer counties, California on September 8, 2022. The Mountain fire was initiated on September 2, 2022 and burned over 13,400 acres in rugged terrain. Critical fire weather conditions began on September 2 persisting into September 6 where the fire exhibited extreme fire behavior and growth on the western flank between September 3-6. Several flights with the SWIS instrument were made on September 3 over the western flank of the fire between 2022-09-03 22:59 and 23:54UTC (1559 to 1654 local time) covering eleven overpasses in 55 minutes with an average return interval of approximately 5 minutes. The Mosquito fire began September 6, 2022 burning over 76,000 acres. During critical fire weather conditions, the fire exhibited extreme fire behavior on September 7-8 expanding towards the northeast, east, and southeast. Flights covering the northeastern, western, and southeastern flank of the fire were made on September 8 during the period of extreme behavior between 2022-09-08 20:27 and 2022-09-09 02:18UTC (09-08 1327 to 1918). Eight repeat passes over the fire during that period were previously processed and used in this analysis.

3.3.2 Data processing

A processing workflow of the IR images included extracting the frames from the thermal bands, collocating image times with camera orientation and GPS, georeference frames, calculating FRP, and automated delineation of active fire edges.

3.3.2.1 Mountain fire - sensor integration, georeferencing, and FRP

Frames recorded in the thermal band during the Mountain fire were extracted separately from the Telops and Workswell cameras, taking two frames per second. Examples of the images in Figure 11 provide a visual of the advantage in using two different band spectrums. MWIR images (Figure 11c) provide more detail about the fire while LWIR images (Figure 11a,b) provide more detail about the background landscape. Two frames per second helped to reduce processing time but still provided enough spatial information to correctly georeference the images.

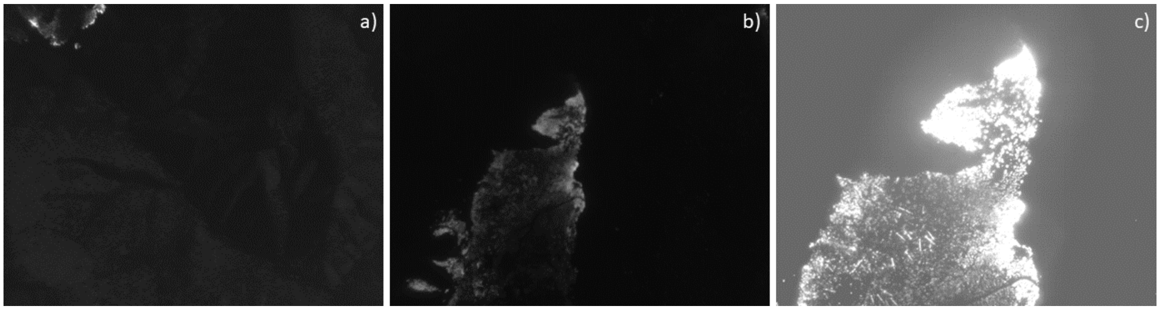

Figure 11. Example of LWIR images (a,b) captured from the Workswell camera and a MWIR image (c) captured from the Telops camera taken during the Mountain fire.

Sensor capture times between the Telops, Workswell, and INS were recorded individually, so the offset between the capture times was retrieved and the camera data was adjusted to match the time of the INS. Raw INS data was processed in the software Qinertia to generate flight paths with internal and external camera orientation. Capture times and camera frames for each camera were then spatially paired with interior camera orientation parameters and navigation coordinates for each timestamp. Output files were generated with roll, pitch, yaw, latitude, longitude, altitude, and standard deviations for the frames. Figure 12 is a geographic overlay of the flight paths taken by the aircraft over the Mountain fire (left) and the Mosquito fire (right) during the time of observations. Flight paths are in white and the evolution of the fire perimeters are in darker (perimeter the day of) and brighter red (perimeter leading into the following day) colors. Flight paths are outputs of the generated flight paths from Qinertia, and the fire perimeters were downloaded from the National Interagency Fire Center (NIFC 2018) open data site (https://data-nifc.opendata.arcgis.com/).

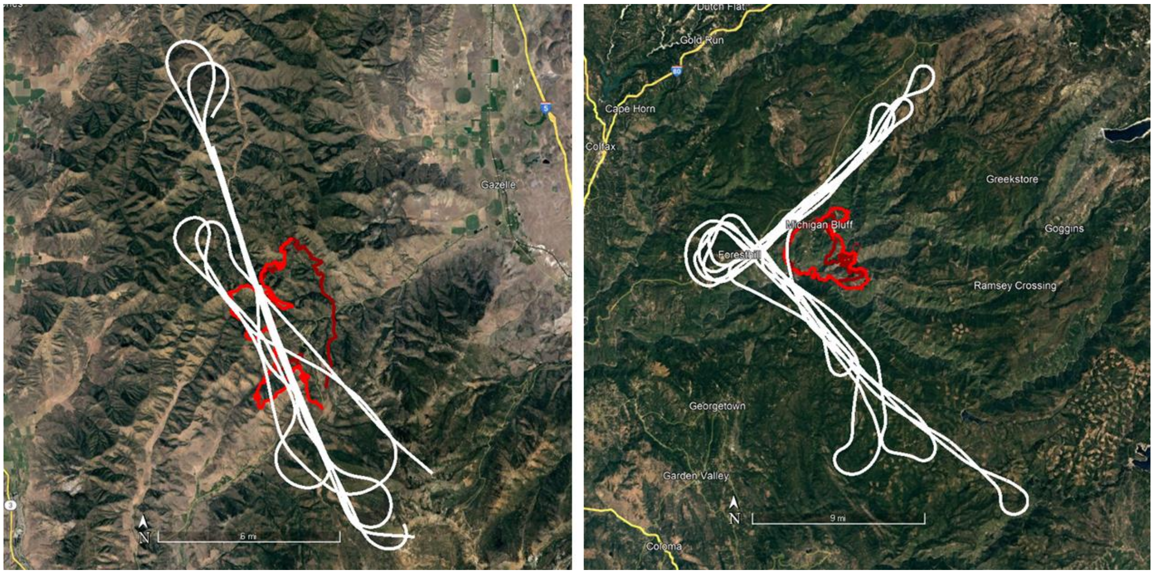

Figure 12. Shows the flight paths (white) taken during the analysis period over the fire perimeters of the Mountain fire (left) and Mosquito fire (right). The darker red perimeters are the fire perimeters on the day of observation and the brighter red perimeters indicate the growth of the fires into the following day.

Fire frames from the Telops and Workswell were imported into the Agisoft Metashape software where they were linked with the camera orientation and navigation reference data. Image pixel values were rescaled to 8-bit type for processing in the georeferencing software, where the maximum BT was assigned a value of 255 and the minimum BT was assigned 0. Frames were organized by passover, so images containing fire were grouped together for each time the aircraft passed over the active fire edge. Images in each group were aligned sequentially to match point features belonging to multiple images. A digital elevation model (DEM) acquired from the United States Geological Survey (USGS 2023) GIS data download portal (https://www.usgs.gov/the-national-map-data-delivery/gis-data-download) was input into the software and overlayed with each of the image groups. Every passover group was then georeferenced to build eleven orthomosaic Geotiffs and exported as two-band array 8-bit types. A visual representation of the georeferencing workflow shows the images aligned on a basemap with projections of point features used to create the alignment in Figure 13.

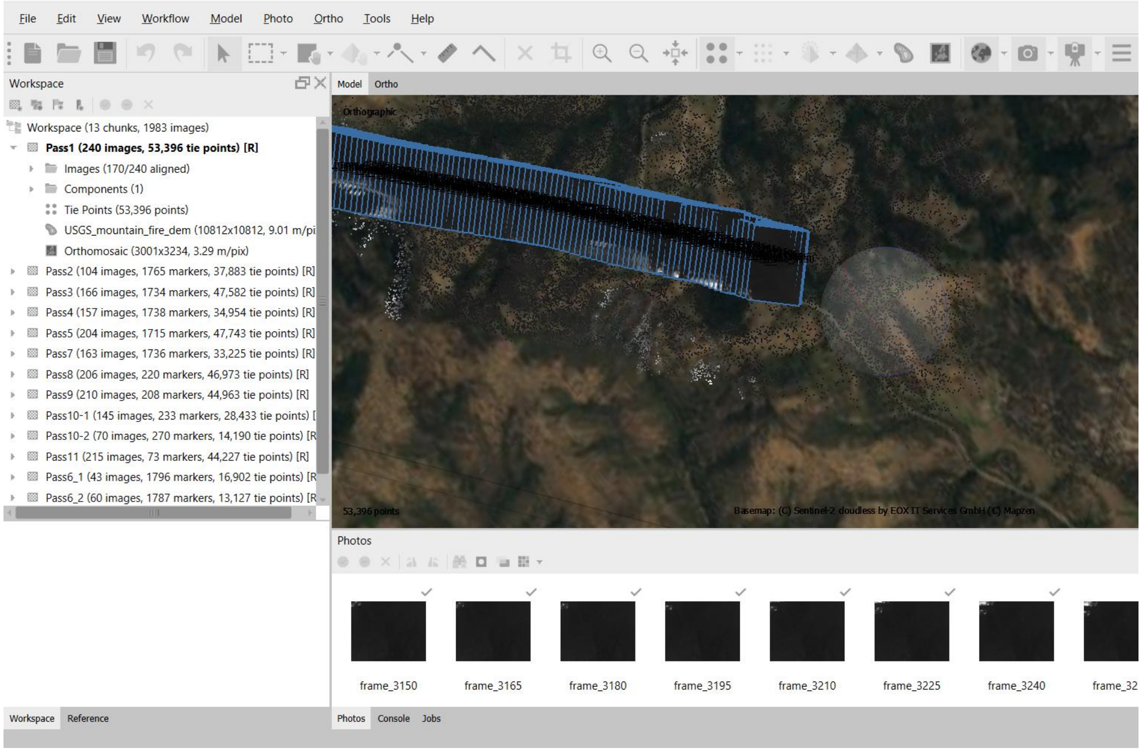

Workspace (13 chunks, 1983 images)
- **Pass1 (240 images, 53,396 tie points) [R]**
  - Images (170/240 aligned)
  - Components (1)
  - Tie Points (53,396 points)
  - USGS_mountain_fire_dem (10812x10812, 9.01 m/pi
  - Orthomosaic (3001x3234, 3.29 m/pix)
- Pass2 (104 images, 1765 markers, 37,883 tie points) [R]
- Pass3 (166 images, 1734 markers, 47,582 tie points) [R]
- Pass4 (157 images, 1738 markers, 34,954 tie points) [R]
- Pass5 (204 images, 1715 markers, 47,743 tie points) [R]
- Pass7 (163 images, 1736 markers, 33,225 tie points) [R]
- Pass8 (206 images, 220 markers, 46,973 tie points) [R]
- Pass9 (210 images, 208 markers, 44,963 tie points) [R]
- Pass10-1 (145 images, 233 markers, 28,433 tie points) [
- Pass10-2 (70 images, 270 markers, 14,190 tie points) [R
- Pass11 (215 images, 73 markers, 44,227 tie points) [R]
- Pass6_1 (43 images, 1796 markers, 16,902 tie points) [R
- Pass6_2 (60 images, 1787 markers, 13,127 tie points) [R

Figure 13. Frames from a single pass over the active fire edge are aligned with tie points (white, gray, and black dots) projected onto a basemap in the Metashape software.

Band one of the LWIR and MWIR mosaic rasters were read into python as an array using the gdal function and inversely rescaled to the maximum and minimum brightness temperatures of the original images. New JPG images of the mosaics were saved with the georeferenced brightness temperature data. Brightness temperatures were used to calculate the per-pixel value of FRP based on the Stefan-Boltzmann Law:

$$FRP_{pixel} = \varepsilon\sigma(BT_{pixel}^{4} - BT_{b}^{4}) \tag{10}$$

FRP_{pixel} is the FRP value per pixel (W/m^2), ε is the emissivity, σ is the Stefan-Boltzmann constant 5.6703×10^{-8} ($W/m^2 \cdot K^4$), BT_{pixel} is the brightness temperature of a pixel, and BT_b is the brightness temperature of the background 296.15K. The Workswell camera uses an emissivity value of 0.95 in its conversion to brightness temperature, so an emissivity value of 0.95 is used in the FRP equation. A pixel was determined to be a fire pixel when BT exceeded 303K, therefore the background value (BT_b) was determined by examining a sample of frames with various amounts of background and fire pixels and taking the mean of the pixel values between the minimum recorded BT and 303K.

3.3.2.2 Mosquito fire - automated edge detection

Building from the automated active fire edge extraction method developed in Chapter 2, this is an attempt to improve and simplify the processes involved in the workflow for this dataset. While the application of a threshold mask can define a transition between identifying the fire area versus the non-fire area and creating a distinct binary edge to be contoured, it does not take full advantage of the sophisticated algorithm of the canny edge detector. The previous method, thresholding around the mean pixel intensity plus canny edge detection, is also dependent on several iterations of multiple morphological functions, and improving the method includes reducing the number of functions used or the number of iterations needed. LWIR orthomosaics created in the Metashape software for the Mosquito fire were used to enhance the automated method in this analysis.

Orthomosaics were previously processed and available to analyze. Each 8-bit LWIR mosaic raster is read using the gdal function as an array using the first of the two bands. A Gaussian filter is applied to the image using a 7x7 matrix and a standard deviation that is determined by the matrix kernel as in Eq. (6). The higher resolution images captured with the SWIS instrument detect a higher variation of fire intensity pixels than the LWIR images used in Chapter 2, so smoothing the image with a larger 7x7 kernel helped to diminish the increased number of gradients for the edge detector to follow. The canny edge detector was then performed on the Gaussian smoothed image with a lower threshold value of 150, an upper threshold value of 240, and the size of the Sobel kernel set to 3. Threshold values were manually tuned until the best possible results were achieved. A lower threshold value of 150 was selected because the edge detector was detecting the edge of the mosaic. Values lower than 150 all edged not only the fire edge but also the mosaic edge. An upper threshold value of 240 did not provide a single continuous edge around the active fire area but provided a significant enough number of smaller edges around the fire area without overedging the frame.

Following the canny edge detector was a single iteration of dilation to make the edges more pronounced and easier to work with. Edges smaller than 20 pixels in size were removed to eliminate any excess edges. Given that the extracted fire edge was comprised of smaller edges following the fire geometry, a function was needed to connect the non-continuous edges. To do so, contours were identified in the image with their left, right, top, and bottom-most coordinates. Each contour compared the distance of neighboring contours to find the minimum distance between it and another contour. Once a minimum distance was determined, a line was drawn to connect those two contours. The final result is a line outlining the active fire edge overlayed on the original mosaic. A block diagram of the new automated method is illustrated in Figure 14.

Figure 14. Block diagram of the automated method developed for the high-resolution LWIR image mosaics during the Mosquito fire. The input image is a long-wave thermal orthomosaic where a Gaussian filter was first applied, followed by the canny edge detector to detect the active fire edges, and then connecting the edge contours.

3.4 Results

3.4.1 Mountain fire, georeferencing and FRP

Georeferenced LWIR orthomosaics were successfully generated in the Metashape software for ten of the eleven repeat passes over the Mountain fire, however the MWIR images experienced difficulty in the processing workflow. This discrepancy was expected with MWIR images given their lack of background detail. Similar point features between images with no background information were difficult to identify, so not all of the images were able to successfully align or the image points were not successfully projected onto the basemap surface. A lack of image alignment with correct projections generated a distorted mosaic, as seen in Figure 15. Therefore, MWIR frames were disregarded for the analysis. FRP can still be calculated from the MWIR data, but without geographic information regarding the pixels, FRP values cannot be properly referenced or integrated with the LWIR data. Important to note is that even though the MWIR frames were unable to be georeferenced in this methodology, it does not imply they are incapable of being georeferenced, rather it accentuates the need for a georeferencing software able to process this type of data.

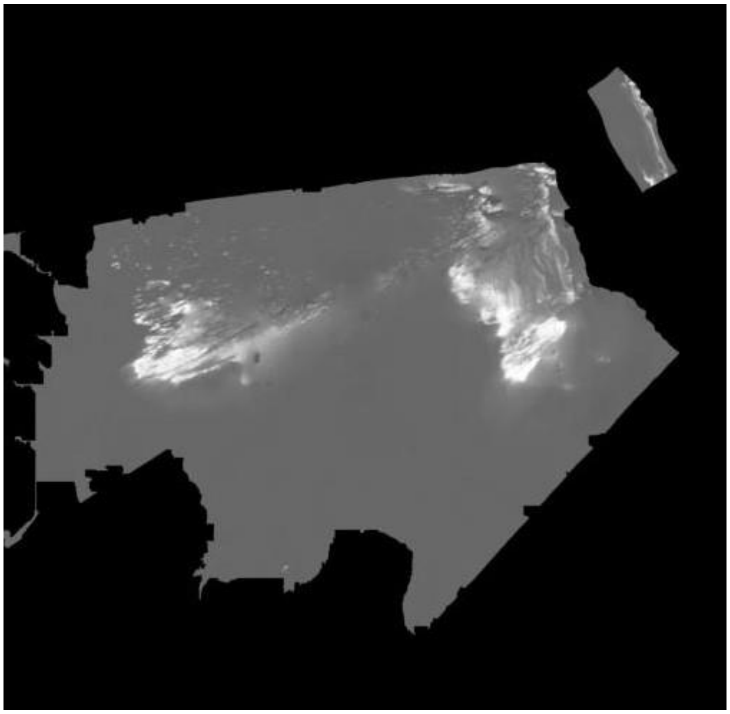

Figure 15. Orthomosaic of MWIR images captured during the Mountain fire. A mosaic raster is produced distorting the fire pixels in the image giving the active fire edge and area a smeared appearance.

Several examples of the successful ten LWIR orthomosaics are shown in Figure 16. The images were properly aligned and an evident representation of the fire geometry and intensity can be seen. During pass six over the fire, there was an inconsistency in the Workswell capture causing a loss of continuity in the fire images. Disparity in image alignment created distortion similar to that seen in Figure 15, so that pass was also disregarded in this analysis. A geospatial composite of the mosaics made in QGIS illustrates a visual of the fire progression (Figure 17). There is a noticeable expansion of the fire along the western front with fire growth in the upper region of the fire, and considerable growth westward in the middle and lower regions following Noyes Valley Road and towards Meadow Gulch. The fire experienced the most significant growth in the middle region on 09-03 between pass 5

23:17:01UTC (1617 local time) and pass 7 23:27:28UTC (1627 local time), and in the lower region between pass 8 23:35:21UTC (1635 local time) and pass 11 23:52:34UTC (1652 local time). Areas that experienced more significant fire behavior coincide with the most intense areas of the fire. Marking Gazelle Calahan Road (the road just east of the lower region of the fire) as a reference point, it can also be observed that the mosaic georeferencing was inconsistent in precision as the distance between the road and fire fluctuates throughout the evolution of the mosaics.

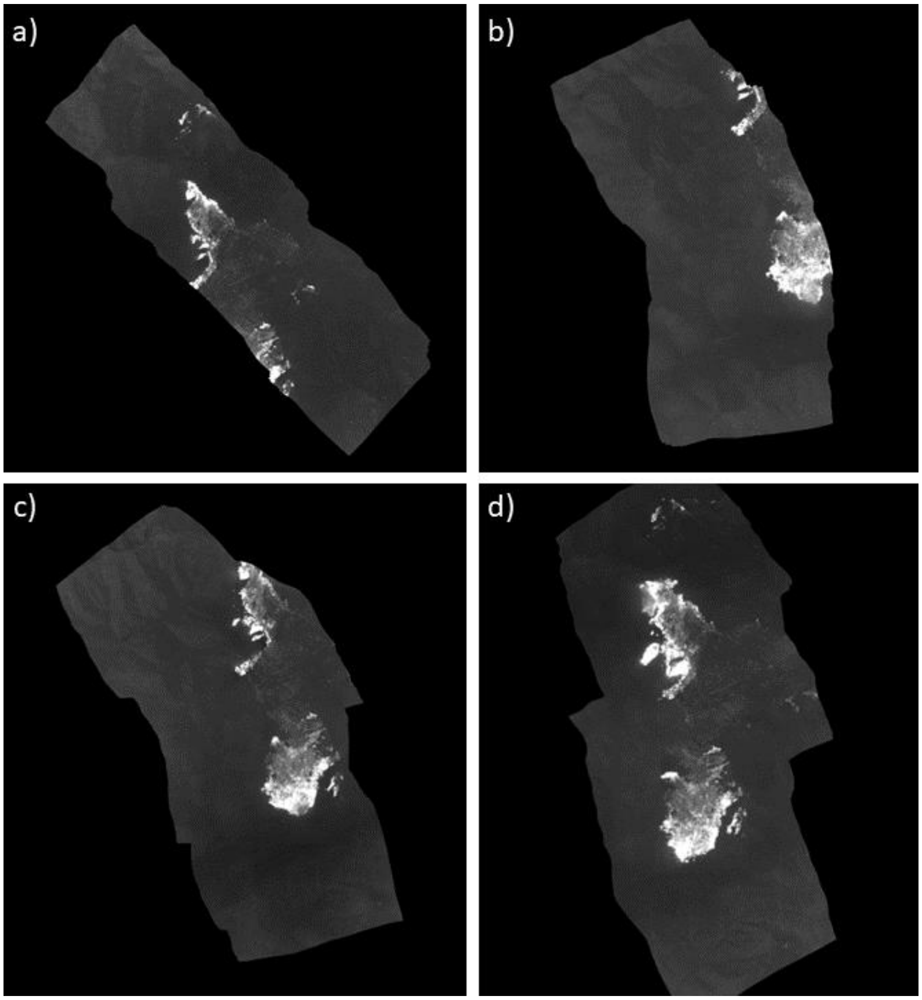

Figure 16. LWIR orthomosaics of four passes over the fire: a) pass 1, b) pass 2, c) pass 4, and d) pass 7. Images are properly aligned without distortion to the shape or size of the fire.

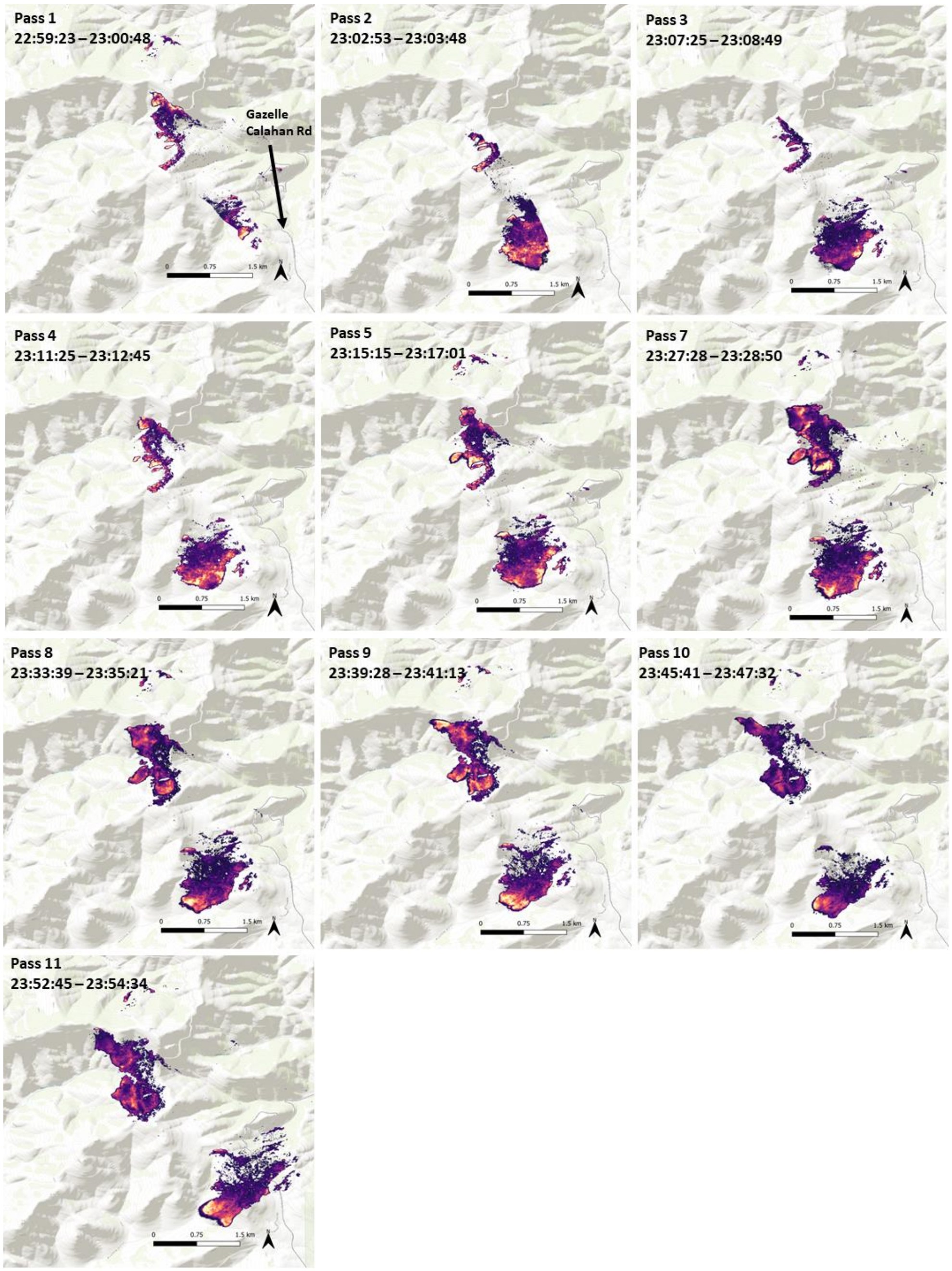

Figure 17. Orthomosaics of the ten passes over the fire show the evolution of the fire spread on 09-03-202 from 22:59:23 – 23:54:34UTC (1559 to 1654 local time). Darker colors indicate lower pixel intensities and brighter white pixels indicate higher pixel intensities. The middle and bottom regions of the fire expanded west/southwestward exhibiting significant fire growth during the 55 minutes of observation. The underlying basemap is the ESRI topographical map.

FRP calculated per pixel from the LWIR orthomosaics correlates well with the geospatial mosaic fire intensity composites in Figure 17. Three images in Figure 18 display the active portions of the fire by plotting FRP values. The maximum range in the FRP plots was set to 4.0 kW/m^2 to provide a better visual of the intensity areas. Table 2 gives the maximum FRP values for each pass mosaic. Maximum FRP values reached up to 13.29 kW/m^2 on pass 5, and the most intense regions of the fire are along the western edge where the majority of fire growth occurred. Pass 10 (Figure 18 right) shows the highest intensity of the fire in the lower region as it expands southwesterly during the observed significant period of fire growth. Given that the MWIR captures the peak emittance of fire, and those frames were omitted in the analysis because they were not able to be processed for georeferencing, higher intensity aspects of the fire are not able to be presented. However, FRP calculated from LWIR images still provides valuable information in assessing fire behavior and can permit how changes in fire intensity alter with fire spread.

Table 2. Calculated maximum FRP values for each pass over the Mountain fire.

Pass Number	Max FRP (kW/m^2)
1	8.18
2	11.95
3	7.86
4	5.51
5	13.29
7	5.19
8	8.18
9	11.39
10	12.24
11	5.51

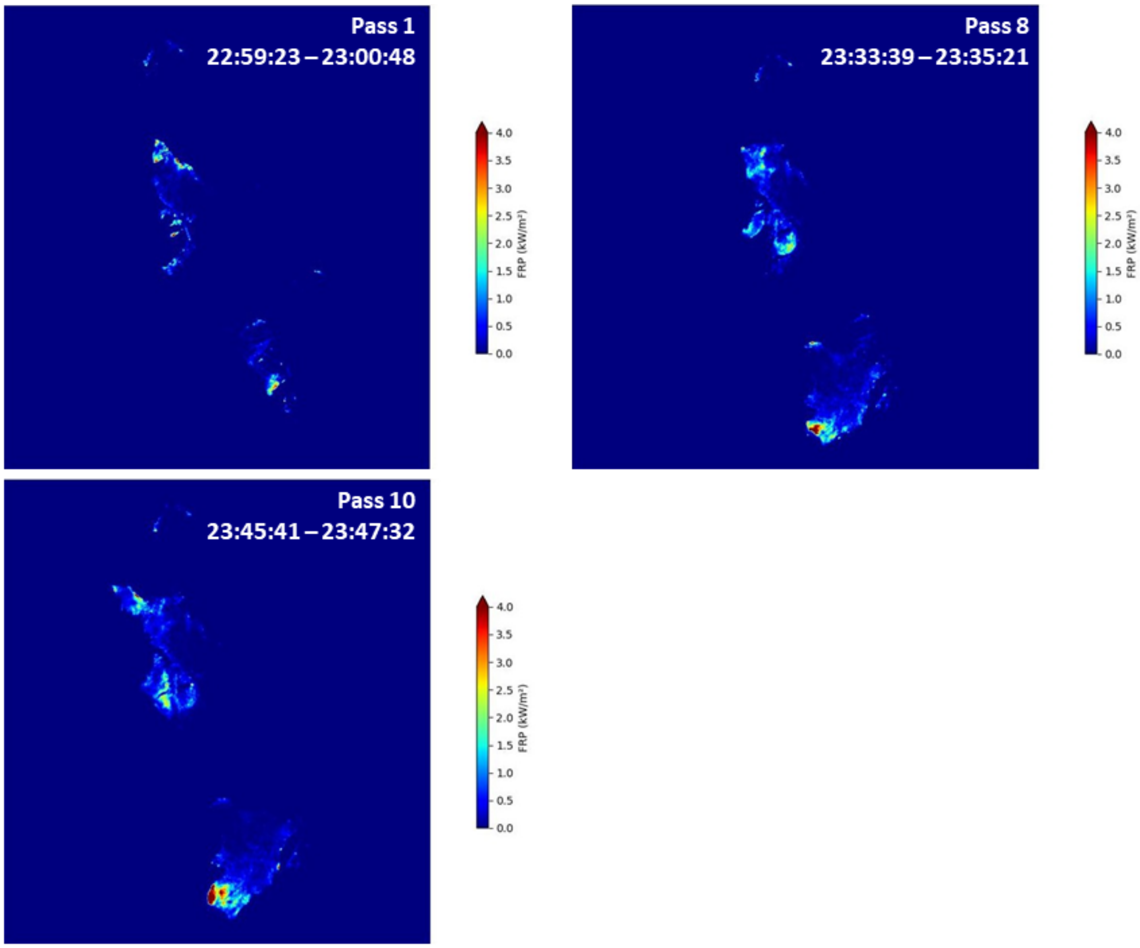

Figure 18. Example LWIR FRP values plotted during pass 1, pass 8, and pass 10 over the Mountain fire 09-03-2022. Higher FRP corresponds to higher intensity areas of the fire along the active fire edge. The FRP value ranges were plotted for visual representation so higher intensity aspects of the fire are clearly displayed.

3.4.2 Mosquito fire, delineating active fire edges

The newly constructed automated active fire edge detection method was applied to the Workswell thermal mosaic images recorded during 8 passes over the Mosquito fire. Adapting previous attempts resulted in the reduction of applying morphological operators, in which the only morphological function used was a single iteration of dilation. Higher-resolution radiometric images allowed for the thresholds in the canny edge detector to be refined, better distinguishing intensity gradients between the background and active fire perimeter. This reduced the extent of the algorithm by several operations. While there was a reduction in the number of operations to the new methodology, the technical aspect of finding and connecting contours can be extensive whereas morphological operators are simple to implement. Even though finding the minimum distance between contour points and connecting contours is standard in connecting non-continuous edges or a set of points, the process may require a deeper analysis of the edges.

Outcomes of the new method can be seen in Figure 19. The new method results in a well-defined edge around the active fire perimeter, handling larger disparities in non-continuous edges such as that in Figure 19f,g. This is valuable because although there is a gap in fire pixels, they may still want to be considered part of the same active fire perimeter. Application of this method may improve previous attempts at creating a single-edge polygon, such as concerning the mosaic of the Creek fire in Chapter 2 that was not used in evaluation metrics because of a large non-continuous edge in the fire perimeter. Further improvements include the reduction of falsely identified background pixels as fire pixels, as no false positives exist outside the fire geometry. Fire area geometries of this dataset are not as complex as the geometries seen in the mosaic images in Chapter 2, nevertheless, they continue to illustrate the variability of geometry in wildfire spread compared to that of experimental or laboratory fires.

Several inconsistencies arise from the new method. In Figure 19a,b several smaller edges were identified inside the fire area and connected to edges along the active fire perimeter. Figure 19c,d,f,g do not contain rogue edges, but rather do not properly identify the nearest contour when connecting points. This may be a proponent of the function miscalculating the

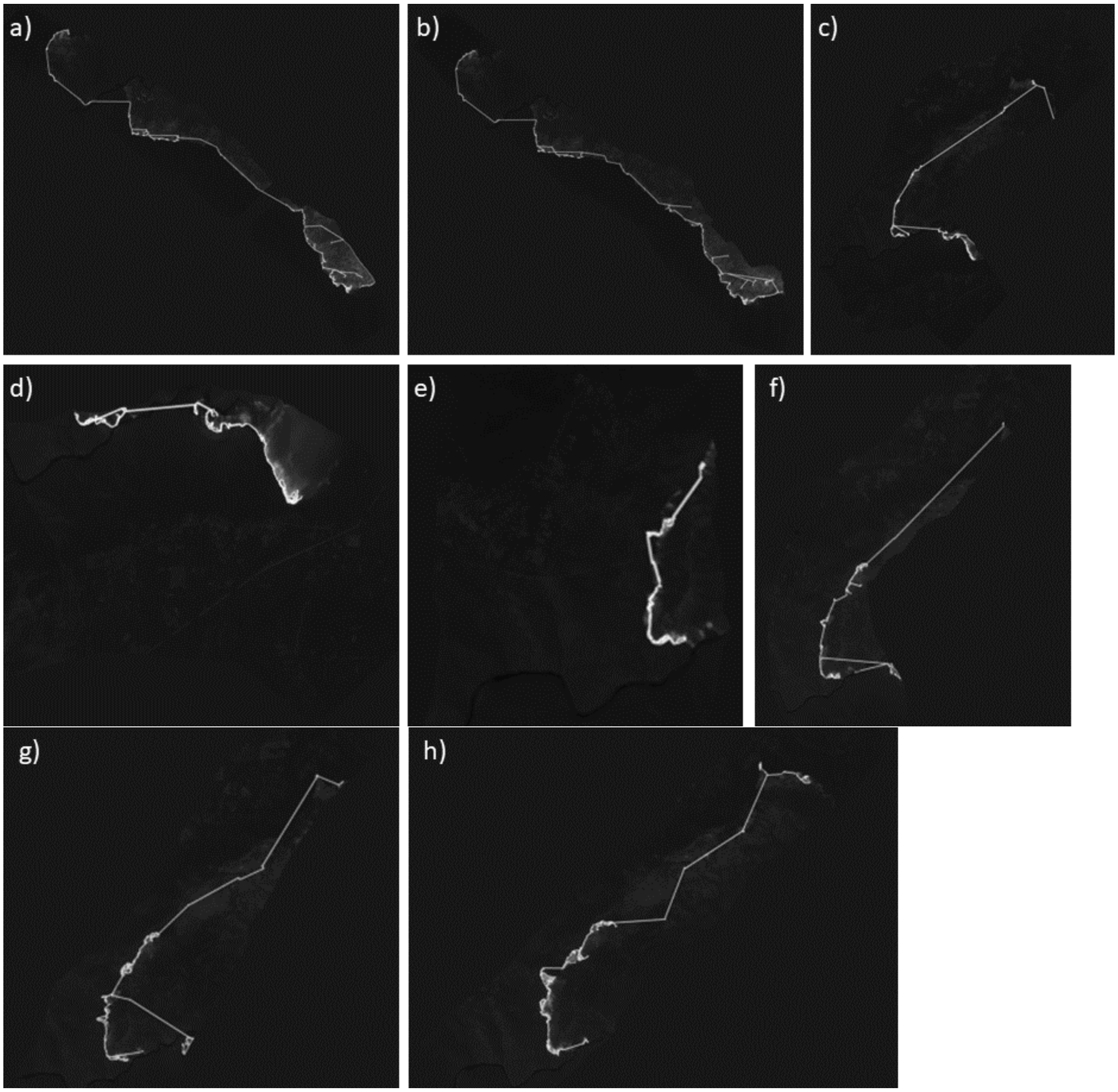

Figure 19. The automated active fire edge method applied to georeferenced flight mosaics. Each mosaic represents one pass over the same fire edge. The algorithm successfully delineated the active fire edge in the eight passes.

minimum distance between two points where it is unable to locate the nearest contour in a specific orientation. Misdirected connected lines appear to be a result of a contour unable to identify a point behind itself. In some instances (Figure 19g,h) the algorithm also cuts inside the fire edge when few fire pixels are present or the gradient between fire and background pixels is weak. Handling the feature would involve changing the threshold values in the canny edge detector which would better identify weak edges, but also lead to an increased number of unwanted edges.

3.5 Conclusion and discussion

The CALFIDE field campaign provided an initial attempt to procure landscape scale high-resolution wildfire data with the SWIS instrument and develop the advanced technical necessary methods to process the data. Successful capture of thermal infrared data during several wildfires including the Mountain and Mosquito fires, allowed for a detailed analysis of the methodology workflow to integrate two different infrared bandpass cameras with an INS, build georeferenced orthomosaics with the LWIR images of repeat passes over the same active fire edge, observe fire spread, calculate FRP, and construct an improved automated method of delineating active fire edges.

Capture times between the two cameras and INS are offset, so before any other processing could be done, the offset was found and matched to the capture time of the INS. Each camera frame was integrated with camera orientation and navigation data. LWIR images of the eleven repeat passes during the Mountain fire were used to successfully generate orthomosaics for ten of the passes and used to show geospatial spread of the fire and calculate FRP. While MWIR images provide higher amounts of detail about the fire, they were unable to be georeferenced because of their lack in detail of the landscape. Not enough tie points between images caused poor alignment creating a distorted mosaic. LWIR data collected during repeat passes over the Mosquito fire were used to improve the automated active fire edge detection method discussed in Chapter 2, where the number of operations in the algorithm was decreased and the active fire edge was satisfactorily contoured with a reduction in the number of falsely identified edges.

High temporal resolution of repeat passes over the same active fire edge was accomplished during this campaign and is an objective that needs to be reiterated. Intentions of processing the times selected in this dataset were to develop advanced methods to integrate two different bandpass cameras used in parallel to calculate FRP via multiple wavelengths in the Plank function (Eq. 2) and observe fire spread. Obtaining detailed information about both the fire and the background within a single frame carries an advantage in the geospatial accuracy of the fire structure and dynamics.

Measuring wildfire characteristics is challenging. High-resolution infrared thermography is a vital component of being able to increase comprehensive datasets available for processing and improve the understanding of fire behavior. Success of the mission is dependent on the operability and performance of the research equipment used, and the ability to fully process the data. The methodology set forth in this analysis contributes to providing a segway into developing advanced methods of processing high-resolution data captured during landscape scale wildfires. Further analysis of fire behavior using this dataset also has the potential to challenge how fire intensity is quantified and how fire behavior can be better represented in numerical models.

3.6 Future work

As this analysis is an initial attempt at developing methods to execute dual band camera integration and processing of an advanced camera system to measure wildfire, and several issues existed in the processing workflow, not everything that was strived for was achieved.

Such is the case in many research campaigns. There is however, the ability to complete the methodology. The primary challenge in this analysis was georeferencing the MWIR images from the Telops with the commercial software used, implying that the pivotal advancement of this project is to develop the software capable of handling this type of data.

Once georeferencing of the MWIR images has been achieved, FRP can be derived by a mutli-band relationship computing temperature from radiance and wavelengths (Riggan et al. 2004). Essentially this would involve inverting the physics of how the cameras measure brightness temperature based on the wavelength to calculate temperature from the Planck function:

$$T = \frac{hc}{k_B \lambda_1 ln\left[\frac{B_2}{B_1}\left(\frac{\lambda_2^5}{\lambda_1^5}\right)\left[exp\left(\frac{hc}{k_B \lambda_2 T}\right)-1\right]+1\right]} \qquad (11)$$

where h is Planck's constant 6.626×10^{-34} (m^2 kg / s), c is the speed of light (3.00×10^{8}m/s), k_B is the Boltzmann constant 1.3808×10^{-23} (m^2 kg / s^2 K), λ_1 and λ_2 are the wavelength of the two cameras in meters, B_2 and B_1 are the radiances ($J/m^{2} \cdot s \cdot sr \cdot \mu m$), and T is the temperature (K). FRP would then be calculated using the Stefan-Boltzmann Law.

Delineating active fire edges from MWIR frames has not yet been attempted in this work, but with the addition of georeferenced MWIR mosaics, there may be an opportunity for a more detailed extraction of the active fire perimeters given that fewer gradients exist between the fire and background. Both the active fire edge methods discussed in Chapter 2 and in this Chapter would be tested. This methodology also has potential to be used in future datasets including the California Canyon Fire Experiment and FireSense campaign.

Conclusion

Wildland fire is a complex physical process that is difficult to quantify. Infrared thermography has become a common method in measuring radiant energy to observe fire spread and calculate fire radiative power to better understand how fires behave. Collection of this type of data is capable of improving fire spread forecasts produced by fire behavior models. Sensors aboard satellites such as MODIS, GOES, and VIIRS provide consistent active fire detection and the means to calculate FRP at large scales, and ground sensors deployed during experimental fires are valuable in measuring the intricacies of fire behavior while providing ground truth. Airborne infrared sensors allow for the capture of fire behavior at higher resolutions than can be achieved by satellites and are more versatile than ground sensors in the conditions they can be deployed under. Operational airborne infrared data used in firefighting management can be a great addition to other research datasets used to advance fire spread analysis. In-situ airborne infrared data acquired during wildfires, such as that obtained from the CALFIDE campaign, can provide invaluable high-resolution insights into fire behavior properties with detailed analysis of fire spread and FRP. The new automated method detailed in Chapter 2 and its refined structure presented in Chapter 3 for extracting active fire edges in infrared images, enhances the capacity to contour the detailed structure of the active fire edge within complex wildfire geometries independent of radiometric properties, is applicable to cameras used during firefighting operations and research, and can be utilized to process large datasets. This provides an opportunity to calculate fire spread at higher resolutions with various camera systems. Analysis of the imagery collected from the SWIS instrument in Chapter 3 establishes the groundwork at developing a state-of-the-art processing methodology for high resolution airborne infrared wildfire data. It demonstrates the capabilities of the new platform in analyzing fire behavior and lays a foundation for automating the entire methodology of georeferencing, extracting active fire edges, and calculating FRP, yet also highlights difficulties in integrating a multi-camera system. As the fire research community strives to advance the collection of wildfire data and the abilities of fire behavior models, improved methodologies to analyze the data will continue to be an important aspect.

References

Agueda, A., Pastor, E., Perez, Y., Planas, E., 2010: Experimental study of the emissivity of flames resulting from the combustion of forest fuels. *International Journal of Thermal Sciences*, **49**, 3, 543-554, https://doi:10.1016/j.ijthermalsci.2009.09.006.

Allison, R. S., Johnston, J. M., Craig, G., & Jennings, S., 2016: Airborne optical and thermal remote sensing for wildfire detection and monitoring. *Sensors (Switzerland)*, **16**, 1310, https://doi.org/10.3390/s16081310.

Arora, S., Acharya, J., Verma, A., and Panigrahi, P. K., 2008: Multilevel thresholding for image segmentation through a fast statistical recursive algorithm. *Pattern Recognition Letters,* **29**, 119-125.

Baddeley, A., 1992: An error metric for binary images. *Robust Computer Vision: Quality of Vision Algorithms*, 59-78.

Cal Fire, 2020: 2020 incident archive. Accessed March 2023, https://www.fire.ca.gov/incidents/2020/.

Canny, J., 1986: A computational approach to edge detection. *IEEE Transactions on Pattern Intelligence and Machine Learning,* **PAMI-8**, 6, 679-698.

Clements, C. B., and Coauthors, 2014: Fire behavior and modeling, *Advances in Forest Fire Research*, Domingos Xavier Viegas, Imprensa da Uniersidade de Coimbra, 392-400.

Clements, C. B., and Coauthors, 2019: The FireFluxII experiment: a model-guided field experiment to improve understanding of fire-atmosphere interactions and fire spread. *International Journal of Wildland Fire*, 28, 308-326, https://doi.org/10.1071/WF18089.

Costa, L. D. F., 2021: Further generalizations of the Jaccard index. *ArXiv*, abs/2110.09619.

Dennison, E. P., Charoensiri, K., Roberts, A. D., Peterson, H. S., Green, O. R., 2006: Wildfire temperature and land cover modeling using hyperspectral data. *Remote Sensing of Environment*, **100**, 212-222, http://doi:10.1016/j.rse.2005.10.007.

Dickinson, M. B., and Coauthors, 2016: Measuring radiant emissions from entire prescribed fires with ground, airborne and satellite sensors - RxCADRE 2012. *International Journal of Wildland Fire*, ***25***, 1, 48–61, https://doi.org/10.1071/WF15090.

Dozier, J., 1981: A Method for Satellite Identification of Surface Temperature Fields of Subpixel Resolution. *Remote Sensing of Environment,* **11**, 221-229.

Duane, A., Castellnou, M., and Brotons, L., 2021: Towards a comprehensive look at global drivers of novel extreme wildfire events. *Climate Change*, **165**, 43, https://doi.org/10.1007/s10584-021-03066-4.

Giglio, L., Schroeder, W., and Justice, C. O., 2016: The collection 6 MODIS active fire detection algorithm and fire products. *Remote Sensing of Environment*, **178**, 31–41, https://doi.org/10.1016/j.rse.2016.02.054.

Gonzalez, R. C., and R. E. Woods, 2002: *Digital image processing second edition,* Prentice Hall, 519-566.

Hantson, S., Andela, N., Goulden, M. L., and Randerson, J. T., 2022: Human-ignited fires result in more extreme fire behavior and ecosystem impacts. *Nature Communications*, **13**, 2717, https://doi.org/10.1038/s41465-022-30030-2.

Huang, D., Lin, T., and Hu, W., 2011: Automatic multilevel thresholding based on two-stage OTSU's method with cluster determination by valley estimation. *International Journal of Innovative Computing, Information and Control,* **7**, 10, 5631-5644, .

Hudak, A. T., Dickinson, M. B., Bright, B. C., Kremens, R. L., Loudermilk, E. L., O'Brien, J. J., Hornsby, B. S., and Ottmar, R. D, 2016: Measurements relating fire radiative energy density and surface fuel consumption - RxCADRE 2011 and 2012. *International Journal of Wildland Fire*, ***25***, 1, 25–37, https://doi.org/10.1071/WF14159.

Hulley, G. C., Ghent, D., Göttsche, F. M., Guillevic, P. C., Mildrexler, D. J., & Coll, C., 2019: Land surface temperature, *Taking the Temperature of the Earth*, P.S. Hulley C. G., Ghent, D., Elsevier, 57-127, https://doi.org/10.1016/b978-0-12-814458-9.00003-4

Jaccard, J., 1901: Distribution de la flore alpine dans le bassin des dranses et dans quelques r´egions voisines. *Bulletin de la Soci´et´e Vaudoise des Sciences Naturelles*, **37**, 241–272.

Johnson, D. G. 2017: Thermal sensors, *Comprehensive Remote Sensing*, P.S. Liang, S., Elsevier, 376-411.

Johnston, J., Wooster, M., Lynham, T., 2014: Experimental confirmation of the MWIR and LWIR grey body assumption for vegetation fire flame emissivity. *International Journal of Wildland Fire*, **23**, 4, 463-479, http://dx.doi.org/10.1071/WF12197.

Johnston, J., Wooster, M., Paugam, R., Wang, X., Lynham, T., Johnston, L., 2017: Direct estimation of Byram's fire intensity from infrared remote sensing imagery. *International Journal of Wildland Fire*, **26**, 8, 668-684, https://doi.org/10.1071/WF16178.

Kochanski, A. K., Mallia, D. V., Fearon, M. G., Mandel, J., Souri, A. H., & Brown, T., 2019: Modeling wildfire smoke feedback mechanisms using a coupled fire-atmosphere model with a radiatively active aerosol scheme. *Journal of Geophysical Research: Atmospheres,* **124**, 9099–9116, https://doi.org/10.1029/2019JD030558.

Kochanski, A. K., Herron-Thorpe, F., Mallia, D. V., Mandel, J. and Vaughan, J. K., 2021: Integration of a coupled fire-atmosphere model into a regional air quality forecasting system for wildfire events. *Frontiers Forest Global Change,* **4**, 728726, doi: 10.3389/ffgc.2021.728726.

Loboda, T. V., and Csiszar, I. A., 2007: Reconstruction of fire spread within wildland fire events in Northern Eurasia from the MODIS active fire product. *Global and Planetary Change*, **65**, 258-273, https://doi:10.1016/j.gloplacha.2006.07.015.

Lentile, L. B., Holden, Z. A., Smith, A. M. S., Falkowski, M. J., Hudak, A. T., Morgan, P., Lewis, S. A., Gessler, P. E., & Benson, N. C., 2006: Remote sensing techniques to assess active fire characteristics and post-fire effects. *International Journal of Wildland Fire*, **15**, 3, 319–345, https://doi.org/10.1071/WF05097.

Martìnez-de Dios, J. R., Merino, L., Caballero, F., and Ollero, A., 2011: Automatic forest-fire measuring using ground stations and unmanned aerial systems. *Sensors*, **11**, 6328-6353.

Monedero, S., Rameriz, J., and Cardil, A., 2019: Predicting fire spread and behavior on the fireline. Wildfire Analyst pocket: A mobile app for wildland fire prediction. *Ecological Modeling,* **392**, 103-107, https://doi.org/10.1016/j.ecolmodel.2018.11.016.

National Interagency Fire Center, 2018: NIFC open data site. Accessed 10 December 2023, https://data-nifc.opendata.arcgis.com/.

O'Brien, J. J., Loudermilk, E. L., Hornsby, B., Hudak, A. T., Bright, B. C., Dickinson, M. B., Hiers, J. K., Teske, C., and Ottmar, R. D., 2016: High-resolution infrared thermography for capturing wildland fire behaviour: RxCADRE 2012. *International Journal of Wildland Fire*, **25**, 1, 62–75, https://doi.org/10.1071/WF14165.

Ononye, E. A., Vodacek, A., and Saber, E., 2007: Automated extraction of fire line parameters from multispectral infrared images. *Remote Sensing of Environment*, **108**, 179-188, https://doi:10.1016/j.rse.2006.09.029.

Otsu, N., 1979: A threshold selection method from gray-level histograms. *IEEE Transactions on Systems, Man, and Cybernetics,* **SMC-9**, 1, 62-66.

Pastor, E., Àgueda, A., Andrade-Cetto, J., Muñoz, M., Pérez, Y., and Planas, E., 2006: Computing the rate of spread of linear flame fronts by thermal image processing. *Fire Safety Journal*, **41**, 569-579, https://doi:10.1016/j.firesaf.2006.05.009.

Paugam, R., Wooster, M. J., and Roberts, G., 2013: Use of handheld thermal imager data for airborne mapping of fire radiative power and energy and flame front rate of spread. *IEEE Transactions on Geoscience and Remote Sensing*, **51**, 6, 3385–3399, https://doi.org/10.1109/TGRS.2012.2220368.

Peterson, D., Wang, J., Ichoku, C., Hyer, E., & Ambrosia, V., 2013: A sub-pixel-based calculation of fire radiative power from MODIS observations: 1. Algorithm development and initial assessment. *Remote Sensing of Environment*, **129**, 262–279, https://doi.org/10.1016/j.rse.2012.10.036.

Peterson, D. and Wang, J., 2013: A sub-pixel-based calculation of fire radiative power from MODIS observations: 2. Sensitivity analysis and potential for weather application. *Remote Sensing of Environment*, **129**, 231-249, http://dx.doi.org/10.1016/j.rse.2012.10.020.

Peterson, D. A., and Coauthors, 2022: Measurements from inside a thunderstorm driven by wildfire: The 2019 FIREX-AQ field experiment. *Bull.Amer.Meteor.Soc.*, DOI 10.1175/BAMS-D-21-0049.1.

Pratt, W. K., 1978: *Digital Image Processing*, John Wiley & Sons Inc, New York, 750 pp.

Radke, L. F., Clark, T. L., Coen, J. L., Walther, C. A., Lockwood, R. N., Riggan, P. J., Brass, J. A., and Higgins, R. G., 2000: The wildfire experiment (WIFE): Observations with airborne remote sensors. *Canadian Journal of Remote Sensing,* **26**, 5*,* 604-417.

Riggan, J. P., Tissell, G. R., Lockwood, N. R., Brass, A. J., Pereira, A. R. J., Miranda, S. H., Miranda, C. A., Campos, T., Higgins, R., 2004: Remote measurement of energy and carbon flux from wildfires in Brazil. *Ecological Applications*, **14**, 3, 855-872.

Riggan, J. P., and Tissell, G. R. 2009: Airborne remote sensing of wildland fires, *Developments in Environmental Science 8*, P.S. Bytnerowicz, A., Arbaugh, M., Andersen, C., Riebau, A., Elsevier B.V., 139-168.

Rudz, S., Chetehouna, K., Sèro-Guillaume, O., Pastor, E., and Planas, E., 2009: Comparison of two methods for estimating fire positions and the rate of spread of linear flame fronts. *Measurement Science and Technology*, **20**, 115501, 10pp.

Rudz, S., Chetehouna, K., Hafiane, A., Laurent, H., and Sèro-Guillaume, O., 2013: Investigation of a novel image segmentation method dedicated to forest fire applications. *Measurement Science and Technology*, **24**, 075403, 8pp.

Schag, G. M., Stow, D. A., Riggan, P. J., Tissell, R. G. and Coen, J. L., 2021: Examining landscape-scale fuel and terrain controls of wildfire spread rates using repetitive airborne thermal infrared (ATIR) imagery. *Fire,* **4**, 6, https://doi.org/10.3390/fire4010006.

Schroeder, W., Ellicott, E., Ichoku, C., Ellison, L., Dickinson, M. B., Ottmar, R. D., Clements, C., Hall, D., Ambrosia, V., & Kremens, R., 2014: Integrated active fire retrievals and biomass burning emissions using complementary near-coincident ground, airborne and spaceborne sensor data. *Remote Sensing of Environment*, **140**, 719–730, https://doi.org/10.1016/j.rse.2013.10.010.

Stephens, S. L., Weise, D. R., Fry, D. L., Keiffer, R. J., Dawson, J., Koo, E., Potts, J., and Pagni, P. J., 2008: Measuring the rate of spread of chaparral prescribed fires in Northern California. *Fire Ecology*, **4**, 1, 74-86, https://doi: 10.4996/fireecology.0401074.

Stow, D. A., Riggan, P. J., Storey, E. J., and Coulter, L. L., 2014: Measuring fire spread rates from repeat pass airborne thermal infrared imagery. *Remote Sensing Letters,* **5**, 9, 803-812, DOI: 10.1080/2150704X.2014.967882.

Stow, D., Riggan, P., Schag, G., Brewer, W., Tissell, R., Coen, J., and Storey, E., 2019: Assessing uncertainty and demonstrating potential for estimating fire rate of spread at landscape scales based on time sequential airborne thermal infrared imaging. *International Journal of Remote Sensing*, **40**, 13, 4876-4897, https://doi.org/10.1080/01431161.2019.1574995.

Toulouse, T., Rossi, L., Celik, T., and Akhloufi, M., 2016: Automatic fire pixel detection using image processing: A comparative analysis of rule-based and machine learning-based methods. *SIViP*, **10**, 647-654, DOI 10.1007/s11760-015-0789-x.

United States Geological Survey: National map-data delivery GIS data download. Accessed October 2023, https://www.usgs.gov/the-national-map-data-delivery/gis-data-download.

Valero, M. M., Rios, O., Mata, C., Pastor, E., and Planas, E., 2017: An integrated approach for tactical monitoring and data-driven spread forecasting of wildfires. *Fire Safety Journal*, **91**, 835-844, http://dx.doi.org/10.1016/j.firesaf.2017.03.085.

Valero, M., Rios, O., Planas, E., and Pastor, E., 2018: Automated location of active fire perimeters in aerial infrared imaging using unsupervised edge detectors. *International Journal of Wildland Fire*, **27**, 4, 241-256, https://doi.org/10.1071/WF17093.

Viedma, O., Quesada, J., Torres, I., De Santis, A., and Moreno, J. M., 2015: Fire severity in a large fire in a Pinus pinaster forest is highly predictable from burning conditions, stand structure, and topography. *Ecosystems,* **18**, 237-250, DOI: 10.1007/s10021-014-9824-y.

Wilson, A. R., Hirsch, N. S., Madden, H. R., and Losensky J., 1971: Airborne infrared forest fire detection system: Final report. *National Technical Information Service*, **INT-93**, 0-114.

Wooster, M. J., Zhukov, B., and Oertel, D., 2003: Fire radiative energy for quantitative study of biomass burning: Derivation from the BIRD experimental satellite and comparison to MODIS fire products. *Remote Sensing of Environment*, **86**, 1, 83–107, https://doi.org/10.1016/S0034-4257(03)00070-1.

Wooster, M. J., Roberts, G., Perry, G. L. W., and Kaufman, Y. J., 2005: Retrieval of biomass combustion rates and totals from fire radiative power observations: FRP derivation and calibration relationships between biomass consumption and fire radiative energy release. *Journal of Geophysical Research Atmospheres*, **110**, 24, 1–24, https://doi.org/10.1029/2005JD006318.

Wooster, M. J., Roberts, G., Smith, A. M. S., Johnston, J., Freeborn, P., Amici, S., and Hudak, A. T., 2013: Thermal remote sensing of active vegetation fires and biomass burning events. *Remote Sensing and Digital Image Processing*, C. Kuenzer, S. Dech., Springer International Publishing, 347–390.

Wooster, M. J., and Coauthors, 2021: Satellite remote sensing of active fires: History and current status, applications and future requirements. *Remote Sensing of Environment*, **267**, https://doi.org/10.1016/j.rse.2021.112694.

Zhang, Y., Li, Q., and Zhou, H. 2016: Theoretical foundation and basic properties of thermal radiation, *Theory and Calculation of Heat Transfer in Furnaces*, Elsevier, 45-74.

Zhukov, B., Lorenz, E., Oertel, D., Wooster, M., and Roberts, G., 2006: Spaceborne detection and characterization of fires during the bi-spectral infrared detection (BIRD) experimental small satellite mission (2001-2004). *Remote Sensing of Environment*, **100**, 1, 29–51, https://doi.org/10.1016/j.rse.2005.09.019.